Wetting and Evaporating Drops on Superhydrophobic Surfaces

by

Masoud Bozorg Bigdeli

A thesis submitted in partial fulfillment of the requirements for the degree of

Master of Science

Department of Mechanical Engineering

University of Alberta

Abstract

Superhydrophobic interfaces, due to their unique water repellent and self-cleaning properties, are attracting a wide-spread interest for implementation in a variety of applications, including self-assembly based fabrication methods, nano/microfluidics, and solar energy harvesting. To facilitate the scaling-up of the superhydrophobic technology and its use in a diverse range of applications, there is a need for further understanding of the wetting and evaporation process of droplets on such surfaces.

The wetting and drying of droplets of pure liquids on hydrophobic surfaces have been extensively studied. On the contrary, the studies concerned with the wetting and evaporation of droplets of complex fluids on superhydrophobic surfaces are still lacking. The objective of this work is to provide experimental data of the wetting states and evaporation dynamics of simple and complex fluids on superhydrophobic surfaces.

Systematic experiments for contact angle measurement of water droplets on superhydrophobic surfaces of different roughness levels have been conducted. Drops placed on surfaces with high roughness values always maintained a none-wetting Cassie-Baster state, while on low roughness level surfaces, droplets rest at a Wenzel wetting state. Drops on surfaces with moderate roughness levels, on the other hand, demonstrated a metastable behavior. Furthermore, the droplets evaporating on these structures revealed a three step process, namely constant contact radius, constant contact angle, and mixed modes, similar to that of microstructured and flat hydrophobic substrates.

Moreover, the wetting and contact angle behavior of aqueous surfactant solutions (0 to 1 CMC) on superhydrophobic microstructures with high and moderate roughness levels

has been studied. The droplets deposited on the high roughness level surface maintained a Cassie-Baxter wetting state for concentrations below 0.5 CMC and a Wenzel state for concentrations above 0.5 CMC. Droplets deposited on the surface with moderate roughness level, however, showed a metastable behavior. For both surfaces, the contact angles of droplets in Cassie-Baxter state were nearly constant with surfactant concentration. The droplets in Wenzel state, adversely, demonstrated a strong dependence on concentration.

Concerning the evaporation of particle laden fluids, aqueous droplets laden with 5wt% and 60wt% of silica nanoparticles were left to evaporate on a microstructured superhydrophobic surface. Low concentration droplets resulted in toroidal light diffracting structures, while quasi-spherical photonic structures were obtained from high concentration droplets. The behavior of droplets was monitored through side and bottom views visualization. From bottom view visualization it was observed that the color of contact area changes from red to green. A Bragg-Snell analysis was conducted to analyze the reflection of the light from the bottom view. The model developed can predict the wavelengths reflected from nanoparticle assemblies made of particles of different sizes and materials.

In brief, this thesis work contributes to better understanding of the wetting and evaporation behavior of some complex fluids on superhydrophobic surfaces of different roughness levels. In particular, additive surfactants and nanoparticles have strong effects on wetting and evaporation behavior at high concentrations.

Preface

The majority of work in this thesis is performed by Masoud Bozorg Bigdeli under supervision of Dr. Peichun Amy Tsai. The work presented in Chapter 2 is done through collaboration. The thesis was presented to Dr. Morris Flynn and Dr. Tian Tang as the examiner committee members.

Chapter 2 of the thesis is partially taken from the journal paper by Adrien Bussonnière, Masoud Bozorg Bigdeli, Di-Yen Chueh, Qingxia Liu, Peilin Chen, and Peichun Amy Tsai, "Universal wetting transition of an evaporating water droplet on hydrophobic micro-and nano-structures." Soft Matter, 13, 5: 978-984, 2017.

Chapter 3 forms a base of a manuscript in preparation by Masoud Bozorg Bigdeli and Peichun Amy Tsai,"Effects of surfactant concentration and surface roughness on wetting of superhydrophobic surfaces", in preparation, 2018.

Chapter 4 is based on a manuscript recently submitted to Scientific Reports: Masoud Bozorg Bigdeli and Peichun Amy Tsai, "Making photonic crystals via evaporation of nanoparticle-laden droplets on superhydrophobic surfaces", submitted, 2017.

Acknowledgements

I would like to express my sincere appreciation to my supervisor Dr. Prichun Amy Tsai whose continuous support and guidance helped me overcome the challenges emerged during the course of this project.

Special thanks go to Elia Neishaboori, my lovely wife, for her unwavering love and support.

I would like to thank my lab mates for providing me a friendly environment to work in. In particular, I thank Adrien Bussonnière for his valuable comments and suggestions on the experiments, and data analysis.

Finally, I am gratefully thankful to my parents for their love, caring and unconditional support during my whole life.

Contents

List of Figures

List of Tables

Chapter 1

Introduction

1.1 Wetting

Wetting, a phenomenon observed in nature and in everyday life, has received notable attention focused on both fundamentals and applications. It plays a key role in diverse industrial processes including heat transfer, oil recovery, lubrication, surface engineering, as well as painting and printing. Recently, there has been a growing interest toward manipulating the wetting properties of surfaces for potential applications in micro and nanofluidics, self cleaning surfaces, oil/water separation and water repellent textiles. Effective tuning of the wetting properties of surfaces for each particular use acquires a fundamental understanding of the phenomena involved.

Contact angle measurement is known to be a facile and useful quantitative approach for studying the wetting behavior of surfaces. The method concerns depositing a droplet on the surface under study and measuring the angle that it forms on that surface.

1.1.1 Wetting on smooth homogeneous surfaces

According to the Young's equation [1], the contact angle of a sessile drop at equilibrium generally relates to the balance of forces among three phases, namely the gas phase, the

liquid phase and the solid phase,

$$\gamma_{sg} = \gamma_{sl} + \gamma_{lg} cos\theta, \tag{1.1}$$

where γ_{sg} is the surface tension at the solid-gas interface, γ_{sl} is the solid-liquid interfacial tension, γ_{lg} is the tension at the liquid-gas interface and θ is referred to as the contact angle.

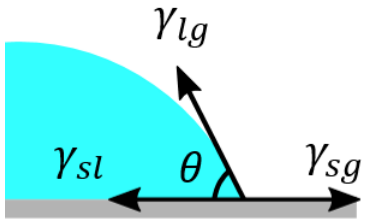

Figure 1.1: Three-phase contact angle as in Young's formulation

1.1.2 Wetting on rough and heterogeneous surfaces

The solid surface is assumed to be ideally smooth and homogeneous in Young's relation, while in practice, surfaces are generally heterogeneous and rough to some extent, influencing the wetting properties. To account for the effect of roughness (r), characterized by the ratio between the entire solid-liquid area beneath the drop and the projected area, Wenzel [2] introduced a model relating the intrinsic contact angle on a smooth surface with apparent contact angle on a rough surface (θ^*) through surface roughness,

$$cos\,\theta^* = r cos\,\theta. \tag{1.2}$$

In this model it is assumed that the droplet completely wets the asperities of the rough surface.

Cassie and Baxter [3], on the other hand, developed a model predicting the apparent contact angle of a droplet placed on a heterogeneous surface. In this model, the apparent contact angle is a weighted average of the intrinsic contact angles on each of the materials forming the surface (θ_1 and θ_2).

$$cos\,\theta^* = f_1\,cos\,\theta_1 + f_2\,cos\,\theta_2, \tag{1.3}$$

where f_1 and f_2 are the fractions of the contact areas that the two materials form with the droplet. Note that, $f_1 + f_2 = 1$.

Considering that air is one of the materials forming the heterogeneous surface, and assuming the intrinsic contact angle at liquid-air interface (θ_2) is 180°, equation (1.3) can be reformulated to equation (1.4)

$$cos\,\theta^* = \Phi\,cos\,\theta + \Phi - 1, \tag{1.4}$$

where θ is the intrinsic contact angle at solid-liquid interface, and Φ is the solid fraction, defined as the ratio between the total area at the solid-liquid interface and its projected area.

For a rough surface that is also heterogeneous, for instance, when the drop is levitating on air pockets, while partially wetting the pillars, equation (1.5) might be used, based on a theoretical work by Marmur [4],

$$cos\,\theta^* = \Phi\,r\,cos\,\theta + \Phi - 1. \tag{1.5}$$

Please note that from this point on, the apparent contact angle is referred to as contact angle and it is shown with symbol θ.

Wenzel and Cassie-Baxter states

The Wenzel (W) and Cassie-Baxter (CB) states of a droplet are presented in Fig. 1.2a and b, respectively. A droplet in W state completely wets the structure, resulting in low contact angles. On the other hand, there is air trapped beneath a droplet in CB state resulting in high contact angle values. For droplets in Cassie-Baxter state resting on superhydrophobic surfaces generally $\theta \gtrapprox 150°$.

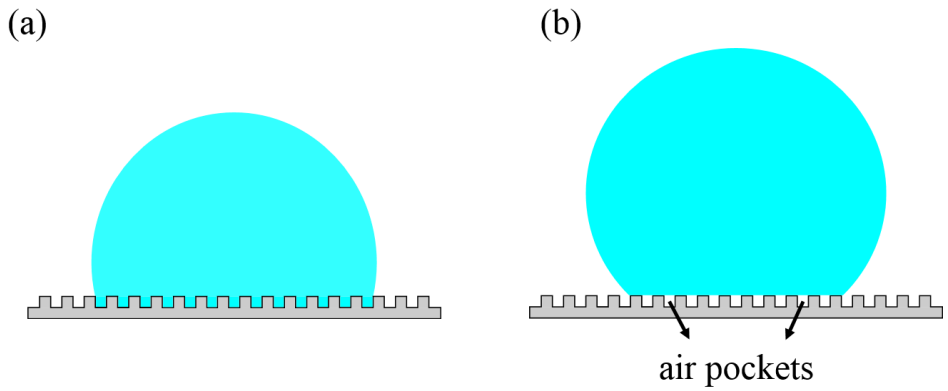

Figure 1.2: (a) Wenzel and (b) Cassie-Baxter wetting states on rough surfaces

Roughness and Solid fraction

For rough surfaces with regular array of pillars, e.g. square and hexagonal arrangements, the roughness and the solid fraction can be evaluated based on the geometrical properties of the surface, Fig. 1.3a and b.

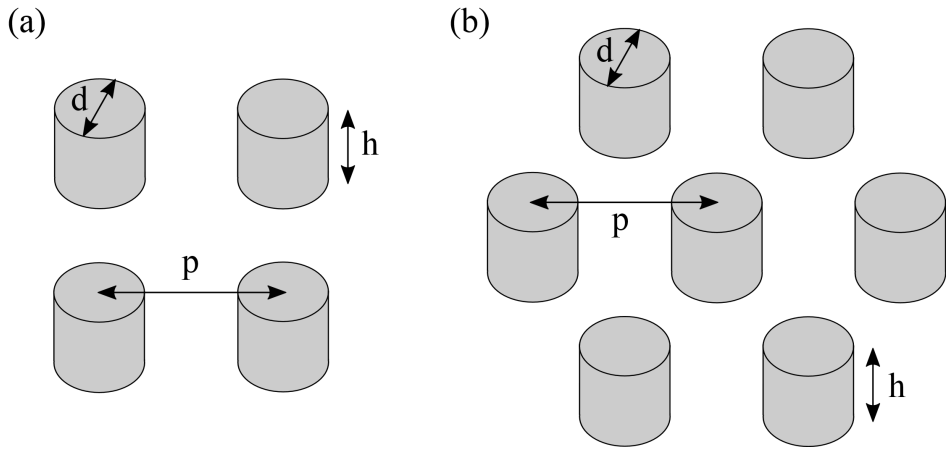

Figure 1.3: (a) Square (b) Hexagonal array of pillars

The roughness (r) and solid fraction (Φ) for square and hexagonal arrangement of the pillars can be evaluated based on Table 1.1. The diameter of the pillars in denoted by d, while h and p are the height and periodicity of the pillars, respectively.

Arrangement	r	Φ
Square	$1 + \frac{\pi dh}{p^2}$	$\frac{\pi d^2}{4p^2}$
Hexagonal	$1 + \frac{2\pi dh}{\sqrt{3}p^2}$	$\frac{\pi}{2\sqrt{3}}\left(\frac{d}{p}\right)^2$

Table 1.1: Roughness and solid fraction of square and hexagonal array of pillars.

1.1.3 Contact angle hysteresis

The difference between the advancing and receding contact angles, denoted as θ_a and θ_r in Fig. 1.4, is called contact angle hysteresis (θ_h). It is a measure of drop mobility on a surface [5], therefore, sticky surfaces are characterized with high θ_h values and conversely for low θ_h values. Superhydrophobic surfaces are normally characterized with low hysteresis values ($\theta_h < 10^\circ$).

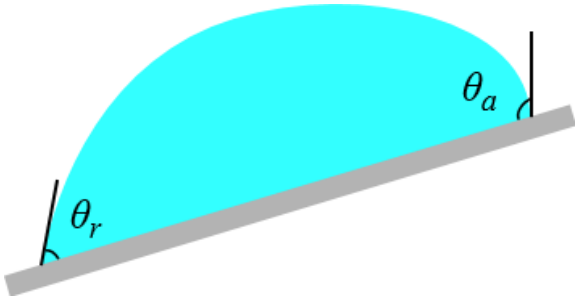

Figure 1.4: Contact angle hysteresis

1.2 Superhydrophobic surfaces

Superhydrophobic (SH) surfaces can be categorized as rough heterogeneous surfaces with relatively high contact angles when compared to hydrophobic ones. These surfaces have been a matter of intense research in the past decades, due to their water repellent and self-cleaning properties. The research on SH surfaces, covers a variety of directions including their potential applications, fabrication methods as well as the experimental and theoretical studies on wetting states and evaporation.

Superhydrophobic surfaces have been under investigation for potential energy-related applications [6], such as anti-icing for photovoltaic cells [7], power lines [8], and aerial vehicles

[9], facilitating dropwise condensation [10] and bubble nucleation [11] for heat exchanger systems, drag reduction and friction control in microfluidic systems [12] and marine vehicles [13].

The fabrication methods of SH surfaces can be grouped into bottom-up, top-down and hybrid approaches [14]. The bottom-up approach, involves building a rough texture on a surface. Vapor deposition, solution growth and colloidal self assembly are examples of bottom-up methods [15]. Top-down approaches include introducing roughness on a surface through processes such as laser ablation and replica molding [16].

Experimental and theoretical studies have been mainly focused on reporting and predicting the wetting and evaporation behavior of fluids on SH surfaces. Moreover, research is being directed towards designing surfaces with robust superhydrophobic features, so that surfaces always maintain high contact angles values. It has been observed that a surface can lose its superhydrophobic properties due to a number of reasons, including contamination of the surface, wear abrasion [17], evaporation [18] and condensation [19] of the working fluid.

More specifically, during evaporation, droplets deposited on superhydrophobic surfaces may not always be able to maintain their non-wetting Cassie-Baxter state and are likely to transit to a wetting Wenzel state. This transition will lead to loss of superhydrophobic property. It has been discussed that an evaporation process can trigger such transition phenomenon, due to decrease in droplet size and the resulting increase of the local internal pressure [20, 18, 21, 22]. Additionally, the geometrical properties of the surface texture have been reported to have an effect on the stability of superhydrophobic features. It has been discussed that, a surface texture consisted of compact arrangement of pillars with higher aspect ratios is more likely to sustain its water repellent properties [23]. Therefore, finer structures might result in increased robustness of SH characteristics. Experiments on wetting and evaporation have been mainly performed on superhydrophobic surfaces with microscale surface features and are normally concerned with a loss of SH properties during evaporation. Moving to an even finer scale, may be beneficial in this case. Due

to fabrication limitations, however, experimental researches on SH surfaces with nanoscale surface geometries are still rare. Researches devoted to the wetting and evaporation process on nanostructured surfaces can reveal useful understandings for design of surfaces with robust superhydrophobic properties, which is the objective of the first project, presented in Chapter 1 of this thesis.

1.3 Complex fluids

The behavior of simple one-component fluids (e.g. water) on superhydrophobic microstructures have been extensively studied. The researches associated with multicomponent complex fluids, on the other hand, are investigated to a lesser extent.

Complex fluids are generally made of two or more components of different phases and/or materials. These fluids normally consist of a component as a continuous phase in which the other components are dispersed. Complex fluids include slurries, pastes, foams, solutions of surfactants, nanoparticle suspensions, emulsions, and many more examples [24, 25] (see Fig. 1.5). In this work, we focus on two types of complex fluids, namely surfactant solutions and nanoparticle suspensions.

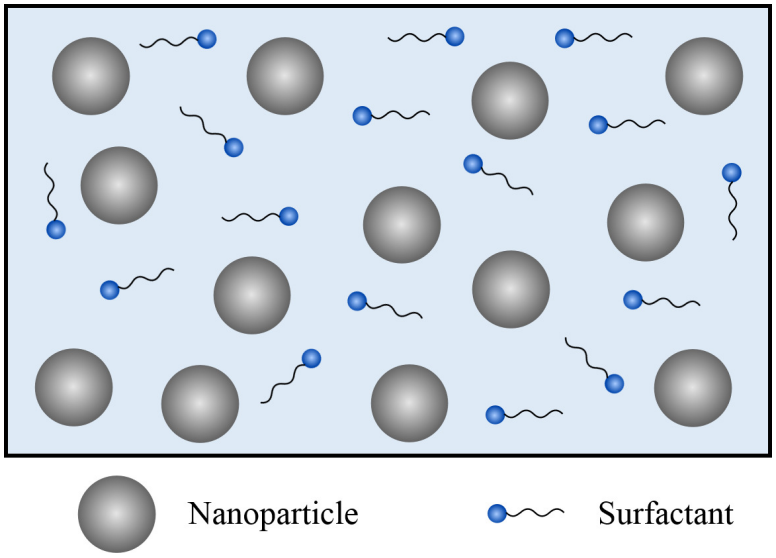

Figure 1.5: A representative complex fluid consisted of dispersions of nanoparticles and surfactants in a simple liquid.

The bulk properties of a complex fluid differ from simple fluids and are rather governed by the properties of its constituents. Careful understating of the phenomena associated with such fluids will provide insights into tailoring their properties for potential biomedical, energy and microfluidic applications.

1.3.1 Surfactant solutions

Surface active agents (also known as surfactants) are molecular structures consisting generally of a hydrophilic head and a hydrophobic head, Fig. 1.6. Owing to their unique bipolar structure, surfactants can be adsorbed at solid-liquid or liquid-gas interfaces, altering the corresponding interfacial tensions.

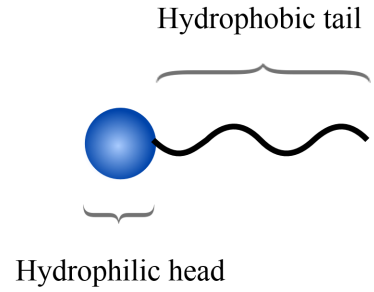

Figure 1.6: Representative molecular structure of a surfactant.

Surfactants are ubiquitous in complex fluids applications. They have been used for dispersing nanoparticles in a base fluid or for mixing immiscible liquids, such as oil and water, forming an emulsion. Moreover, in microfluidic applications, surfactants have been employed to control the coalescence of emulsion droplets [26, 27, 28, 29] and to tune the wetting and spreading of the working fluids [30, 31]. Superhydrophobic surfaces are also being used in micro/nanofluidic devices, due to their ability to improve the fluid movement in microchannels [32, 33, 34]. It has been reported that, in an aqueous surfactant droplet resting on a superhydrophobic surface, the surfactants may adsorb to solid-liquid interface, triggering the transition from a Cassie-Baxter state to a Wenzel state [35, 36]. However, direct experimental evidence on this phenomenon is still lacking. In this regards, the effect of surfactants on wetting on superhydrophobic interfaces needs to be studied through carefully

designed experiments. This motivates a part of the thesis work, presented in Chapter 3.

1.3.2 Nanofluids

Nanofluids are complex fluids synthesized by dispersing one or more types of nanoparticles and or dispersants in a base fluid as the continuous medium. They have been introduced as prospective replacements for conventional heat transfer fluids for the aim of enhancing the efficiency of heat transfer systems [37]. This idea of dispersing nanoparticles within fluids to obtain certain local or global features, is nowadays extended to other application areas, for instance, in hyperthermia [38], drug delivery [39], lubrication [40], and magnetic sealing [41]. Due to their complex nature, the wetting properties and evaporation of the nanofluids may differ from those of simple fluids such as water. For instance, it has been observed that, during evaporation of a nanofluid droplet on a hydrophilic substrate, the nanoparticles tend to self-assemble, forming a two-dimensional ring like structure [42]. On superhydrophobic surface, however, there are only a few studies concerning the evaporation of nanofluids [43]. High contact angle of droplets on SH surfaces, typically results in three-dimensional assemblies [44]. By carefully selecting the size of nanoparticles dispersed, the particle assemblies can be made to diffract light, acting as photonic crystals.

1.3.3 Photonic crystals

Photonic crystals (PhCs) are are structures characterized with periodic variation of dielectric constant. Due to the periodicity of the structure properties, when light enters the crystal, only certain frequencies can be reflected out. This feature can be employed for a variety of applications, including temperature [45] and strain [46] sensors, optical filters [47] and absorbers [48], lasers [49] and superlens [50].

Photonic crystals can be made in one, two and three dimensions, (Fig. 1.7). There is a growing interest towards fabricating 3D PhCs, due to emerging applications in solar energy harvesting. In such cases, the periodicity may be spatially varied to maximize the light harvesting efficiency, resulting in aperiodic photonic crystals [52].

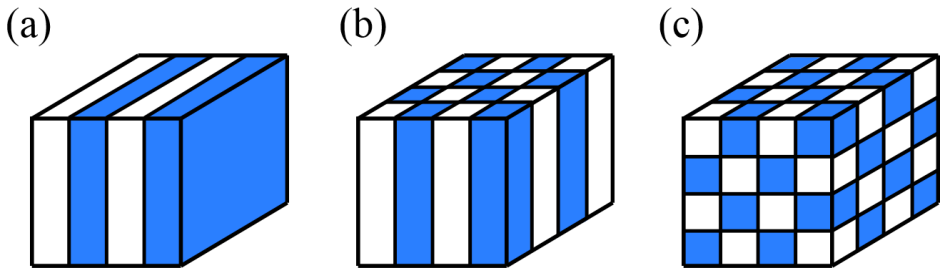

Figure 1.7: Representative photonic crystals (a) one-dimensional (b) two-dimensional (c) three-dimensional. Blue and White are materials with different dielectric constants. Figure inspired from reference [51].

There are two main methods for fabrication of 3D PhCs: the bottom-up method through self-assembly of particles in a colloidal dispersion, and the top-down method based on lithography [53].

Superhydrophobic surfaces, due to the high contact angles, may be useful for fabricating three-dimensional PhCs through bottom-up self-assembly. However, the studies on this topic are rare and not comprehensive. Hence, more detailed investigations are required to investigate the phenomena concerned with self-assembly on SH surfaces, as the topic of current thesis work presented in Chapter 4.

1.4 Overview

The main objective of this thesis is to elucidate the wetting and evaporation dynamics of simple and complex fluids on superhydrophobic surfaces of different geometrical parameters and roughness. The first step toward this objective was the study of wetting and evaporation process of pure droplets on a variety of superhydrophobic nanostructures. Here, the measurements and analysis of contact angle dynamics of pure water on such surfaces are reported (in Chapter 2).

The next step was to study the wetting behavior of complex surfactant solutions of different concentrations on superhydrophobic microstructures of different roughness levels, discussed in Chapter 3. In addition to conventional contact angle measurements via side-

view snapshots of droplets, the effect of surfactant concentration on the wetting state is studied through bottom-view image analysis.

Finally, the wetting and evaporation behavior of nanoparticle-laden droplets is studied on a superhydrophobic surface, described in Chapter 4. It will be shown that, through careful design of experimental parameters, structural photonic crystals can be fabricated.

Chapter 2

Wetting and evaporation of pure water on superhydrophobic surfaces[1]

2.1 Introduction

There has been an emerging interest in improving the surface properties of conventional materials to obtain materials with novel functions [54, 55, 56]. In particular, micro- and nano-textures of hydrophobic surface designs are introduced to achieve higher contact angles with respect to flat substrates. This is inspired by the surface properties of natural organisms, such as plants and insects, where a water droplet forms a distinctively higher contact angles (θ) when compared to typical hydrophobic surfaces [57, 58, 59]. These textured surfaces are referred to as superhydrophobic (SH).

Regardless of plausible potential applications attributed to SH surfaces in literature, surfaces demonstrating robust superhydrophobic features, maintaining an extremely high contact angle, are still rare. This is due to an irreversible wetting transition that can take

[1]The material presented in this chapter is partially based on Bussonnière, A., Bigdeli, M.B., Chueh, D.Y., Liu, Q., Chen, P. and Tsai, P.A., "Universal wetting transition of an evaporating water droplet on hydrophobic micro-and nano-structures". Soft Matter, 13(5), pp.978-984, 2017.

place on SH surfaces, breaking down the water repellent properties. It is well established that, evaporation can trigger the wetting transition [18] from an air-trapping Cassie-Baxter (CB) state [3] to a wetting Wenzel (W) state [2]. A number of methods have been suggested to prevent the transition, ranging from exposing the surfaces to light, heat and vibration, to variation of the chemical and geometrical properties of the surface. More specifically for geometrical properties, it has been reported that, designing the surfaces for pillars with higher aspect ratios and solid fractions may be favorable for a metastable CB state. Hence, finer structures may enhance the durability of the superhydrophobic properties. Wetting and evaporation of droplets have been extensively studied for surfaces with microscale geometrical features. However, there are only a few experimental studies performed on wetting and evaporation on nanostructured SH surfaces.

To conduct such experiments, we have collaborated with a research group expert in materials synthesis [60, 61, 62], which provided us with superhydrophobic surfaces characterized with nanoscale features. Here, the wetting states and evaporation dynamics of water droplets resting on the nanostructured SH surfaces are investigated. The results of this study can contribute to elucidate the relationship between the geometry of surface texture and the contact angle at which the wetting transition occurs.

2.2 Experimental

The superhydrophobic surfaces used in this study are characterized by square arrays of parallel cylindrical pillars. Table 2.1, presents the geometrical properties of the nanostructured surfaces used in this study, where h is the pillar height, p is periodicity, $r = 1 + \frac{\pi dh}{p^2}$ is the roughness and $\Phi = \frac{\pi d^2}{4p^2}$ is the solid fraction. A representative scanning electron microscope (SEM) image of nanostructures and a schematic denoting the square arrangement of pillars are shown in Fig. 2.1a.

The nanostructures were made of silicon and subsequently hydrophobized using trichloro (1,1,2,2-perfluroocytl)-silane. Two cameras were synchronized to capture the side and top views of droplets (10 μl) during the evaporation process. The representative side-view

Surface	h (μm)	p (μm)	d (μm)	r	Φ
W1	1	0.8	0.2	1.98	0.049
W2	1	2	0.4	1.31	0.031
W3	1	2	0.2	1.16	0.008
W4	2	0.8	0.4	4.93	0.196
W5	2	2	0.4	1.63	0.031
W6	2	1	0.4	3.51	0.126

Table 2.1: Geometrical properties of superhydrophobic nanostructures

snapshots of the droplets deposited on surfaces W4 and W3 are presented in Fig. 2.1b and c, respectively. Such snapshots were used to evaluate the droplet contact angle, and base radius using a Matlab code based on a low-bond axisymmetric drop shape analysis method [63]. Top-view snapshots were used to inspect the sphericity of the droplet. The water contact angle on the smooth surface (θ_F) was measured to be 115°. The experiments ran at room temperature (25°C) and 16% of relative humidity.

2.3 Results and Discussion

2.3.1 Wetting states

The initial wetting states of the droplets deposited on superhydrophobic surfaces (W1 to W6) are reported in Fig. 2.1d. The reported results are categorized into stable Cassie-Baxter and stable Wenzel states based on a criteria developed by equating Wenzel and Cassie-Baxter models in equations (1.2) and (1.4) [64] for wetting on rough surfaces that is here reformulated for roughness (r),

$$r = \frac{\Phi - 1}{cos\theta_F} + \Phi, \tag{2.1}$$

Through this equation, the Φ-r space can be separated into regions characterized with different wetting states based on the intrinsic contact angle of the surface. Here, Grey and Black lines correspond to intrinsic contact angles of 109° and 115°, respectively. The prediction suggests stable CB wetting states for $r > \frac{\Phi-1}{cos\theta_F} + \Phi$, that is the reddish area in Fig. 2.1d. In other words, for high roughness surfaces a CB state is expected to be evidenced.

Indeed, a Cassie-Baxter state was observed for droplets deposited on high roughness surfaces (W4 and W6) during our experiments, meaning the droplet stayed on top of the pillars with air entrapped beneath. This suggests that there exists a composite interface beneath the droplet consisting of solid-liquid and liquid-gas interfaces. These droplets resting in CB state, formed initial contact angles larger than 160°. The contact angle of a droplet in CB state is a function of substrate's solid fraction and can be evaluated using equation (1.4) developed by Cassie and Baxter [3].

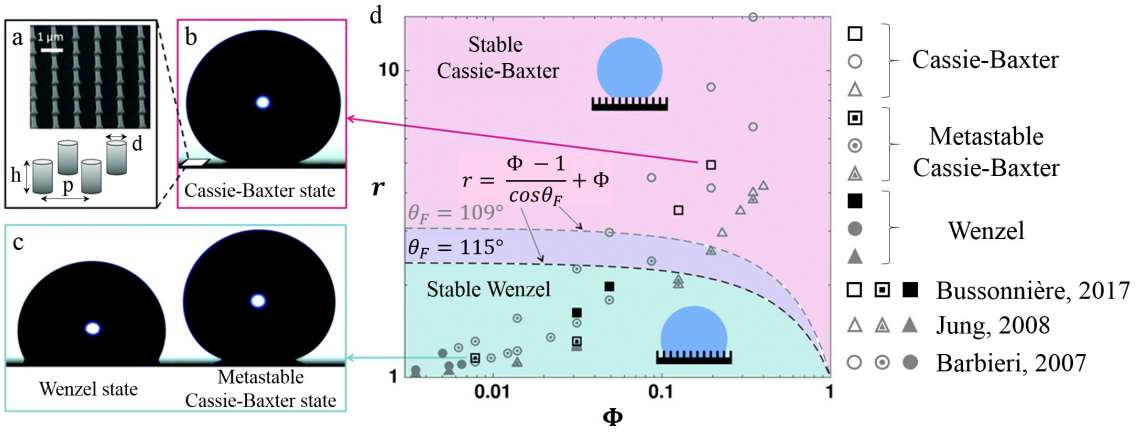

Figure 2.1: (a) SEM image and schematic of the square arrangement of pillars forming hydrophobic nanostructures. (b) Pure water droplet resting on a superhydrophobic nanostructure (W4), with r = 4.93 and Φ = 0.196 in a stable Cassie-Baxter state. (c) Two droplets in Wenzel and metastable Cassie-Baxter states on surface (W3) with r = 1.16 and Φ = 0.008. (d) Wetting state diagram of water droplets developed based on roughness, solid fraction and smooth contact data reported in Bussonniére et al. [65], Jung et al. [66] and Barbieri et al. [67]. Grey and Black dashed lines correspond to intrinsic contact angles of 109° and 115°, respectively. They divide the state diagram into a stable Wenzel state domain (in green), and a stable Cassie-Baxter domain (in red). This criteria is developed by Bico et al. [64] based on interfacial energies. Figure is adopted from [65].

A stable Wenzel wetting state was observed for droplets deposited on surfaces W1 and W5, characterized with moderate roughness values. This is also inline with the prediction of equation (2.1), which predicts the Wenzel state as a more favorable state for low roughness levels, i.e. the green area in Fig. 2.1d. In this case, the droplets completely wet the entire surface texture and formed initial contact angles smaller than 120°. The lower value of the contact angle compared with a drop in CB state is due to the change in the contact area at

solid-liquid interface. The contact angle of a droplet in W state is a function of the surface roughness and can be evaluated through equation (1.2).

Theoretically, stable Wenzel state is more favorable for the droplets deposited on lowest roughness surfaces (W3 and W2). However, if the droplets were deposited carefully using a needle, a Cassie-Baxter metastable state could be achieved. Similar results have been also reported in literature [66, 68]. Such metastable state could be due to a local minimum in surface energy, which can eventually transition to Wenzel state [69, 70].

2.3.2 Evaporation dynamics

The contact radius and contact angle behavior of evaporating water droplets resting on nanostructured surfaces are reported in Fig. 2.2a and b, respectively. In this figure, R_0 is the radius of the free droplet of the same volume, and t_f is the evaporation time until which contact angle and contact radius data is analyzed. The determination of t_f is based on high resolution side-view snapshots (taken at 0.5 fps) with a spatial resolution of 344 pixels/mm, which helps us to accurately estimate t_f. The typical error in t_f is within 1 second, corresponding to an error in t/t_f within 0.04%, an insignificant error. The results correspond to an initial non-wetting CB state (in red) and an initial wetting W state (in blue). In addition, the corresponding filled symbols in Fig. 2.2b depict the initial contact angles of the deposited drops predicted through equations (1.2) and (1.4), for Wenzel (blue) and Cassie-Baxter (red) states, respectively.

Overall the data are consistent with the models. For Wenzel droplets following in equation (1.2), it is theoretically expected to achieve higher contact angles on hydrophobic surfaces with higher roughness levels. Cassie and Baxter's model, equation (1.4), predicts higher contact angles when solid fraction is decreased. Contact angle comparisons of water droplets resting on SH surfaces with a variety of properties are extensively studied in literature and the results are generally in agreement with the Wenzel's and Cassie-Baxter's predictions [71, 72, 73, 74, 75].

Concerning the evaporation dynamics, the data presented in Fig. 2.2a and b shows that

the droplets demonstrated similar behaviors during evaporation on surfaces with different roughness levels. The process can be divided into three stages, namely initial, intermediate and final. During the initial stage, the contact radius remained constant (pinned contact line), whereas the contact angle decreased. The droplet preserved a relatively constant contact angle after reaching the receding contact angle, that was ≈ 155° and ≈ 90° for CB and W stats, respectively. On the other hand, the contact radius of the droplet began decreasing in the course of this intermediate stage. During the final stage, the contact angle and contact radius both had a decreasing trend. The initial stage is known as constant contact radius (CCR) mode, while the intermediate and final stages are recognized as constant contact angle (CCA) and mixed modes in literature [76, 77, 78].

Similar behavior have been also reported for evaporating water droplets resting on microstructured and flat surfaces [79, 80]. Owing to the low contact angle hysteresis of the surfaces studied here, the evaporation of CB droplets mostly follows a CCA mode. Wenzel droplets, on the other hand, experience a mostly CCR mode.

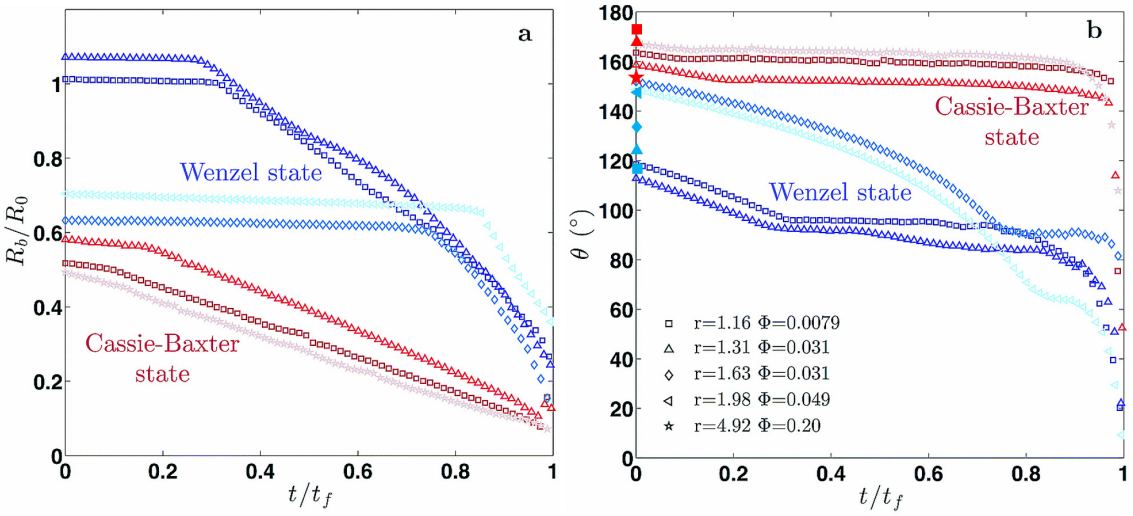

Figure 2.2: (a) Contact radius and (b) contact angle evolution of evaporating water droplets. Droplets in CB state are depicted by △, □ and ☆. The droplets in W state, are depicted by □,△,◇ and ◁. The respective filled symbols denote the theoretical initial contact angles, for W and CB states, determined using equations (1.2) and (1.4), respectively. Figure is adopted from [65].

2.4 Conclusion

The wetting states and evaporation behavior of water droplets resting on nanostructured hydrophobic surfaces with varying geometrical properties were investigated. The droplets deposited on surfaces characterized with high roughness levels, formed a non-wetting Cassie-Baxter wetting state. Whereas, the droplets resting on moderate and low roughness surfaces initially formed a Wenzel wetting state. For surfaces with low roughness values, it was also possible to achieved a metastable Cassie-Baxter state by carefully placing the droplets on substrates using a needle. Finally, the evaporation process for droplets resting on nanostructures was studied. Despite different geometrical features and corresponding wetting states, the droplets demonstrated similar evaporation dynamics for all surfaces. The droplets were initially in a constant contact radius mode, subsequently, followed a constant contact angle regime and finally, underwent a mixed mode. Such behavior has been also reported for droplets evaporating on flat and microstructured surfaces.

Chapter 3

Wetting of aqueous surfactant solutions on superhydrophobic surfaces

3.1 Introduction

Surfactants have been used extensively in micro/nanofluidic systems for controlling the emulsion stability [26, 27, 28, 29] as well as the wettability and spreading properties of working fluids [31, 30]. However, surfactants may occasionally be accumulated in micro/nanochannels resulting in contamination of the system. As regards experiments with superhydrophobic channels, recently, there have been reports indicating discrepancies in experiment results as well as loss of superhydrophobic functionality when using surfactant solutions [81]. Surfactants can likewise affect the contact angle and wetting state on a SH surface. It has been shown that contact angle can drastically change with concentration of surfactants in an aqueous media [82, 35]. Despite that, direct experimental evidences on transition from non-wetting Cassie-Baxter (CB) state to the wetting Wenzel (W) state triggered by surfactant concentration are still lacking.

In this study we have investigated the dependence of contact angle and wetting state

on the surfactant concentration for two superhydrophobic surfaces of different roughness levels. Our study reveals contact angle is nearly constant and high ($\approx 130^\circ - 140^\circ$) at different surfactant concentrations, when the droplet is in CB state. Droplets in W state, however, unveiled strong dependency of contact angle on concentration. The results proved surface roughness as another key factor affecting the wettability properties.

3.2 Experimental

A replica molding process was adopted using Polydimethylsiloxane (PDMS) to prepare the superhydrophobic surfaces. The surfaces were 2×2 cm^2 in area, transparent, and patterned with hexagonal array of parallel cylindrical pillars.

The geometrical properties of the two surfaces used in this study are presented in Table 3.1, where h is the pillar height, p is periodicity, $r = 1 + \frac{2\pi dh}{\sqrt{3}p^2}$ is the roughness and $\Phi = \frac{\pi}{2\sqrt{3}}\left(\frac{d}{p}\right)^2$ is the solid fraction.

Surface	**h** (μm)	**p** (μm)	**d** (μm)	**r**	Φ
S1	4.78	7.73	5.54	2.608	0.466
S2	4.78	14.12	5.51	1.480	0.138

Table 3.1: Geometrical properties of superhydrophobic surfaces

Figure 3.1a presents scanning electron microscope (SEM) image of S1 surface used in this study. It can be observed that the lateral surfaces of the pillars are rough, which is due to the manufacturing process (Reactive Ion Etching) of the molds used here. Such fine roughness could change the overall roughness value of the surface by less than 4%. As a result for a Cassie-Baxter droplet, this ripple roughness would contribute negligible effect to the wetting. A representative snapshot of a 10 μl milli-Q water droplet on S1 surface is provided in Fig. 3.1b.

Aqueous solutions of sodium dodecyl sulfate (SDS), with critical micelle concentration (CMC) = 0.082 mM, were prepared for 9 different concentrations (0.02, 0.05, 0.1, 0.2, 0.25, 0.33, 0.5, 0.75 and 1 CMC). For each concentration, unless otherwise noted, 9 tests were performed on a freshly made SH surface. All experiments were pursued at relative humidity

of 18 ± 2% and room temperature, 23 °C.

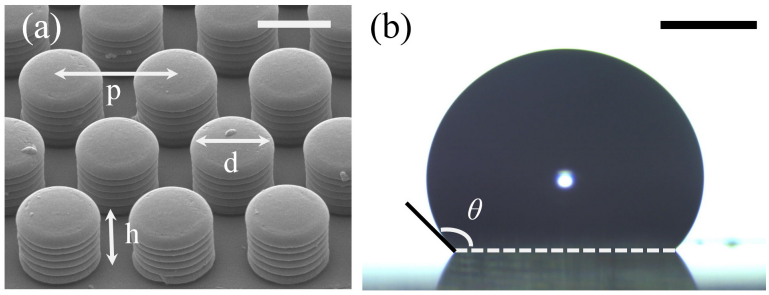

Figure 3.1: (a) SEM image of a superhydrophobic surface texture. Scale bar corresponds to 5 μm. (b) Side view of water droplet on the SH surface with $\theta \approx 130°$. Scale bar corresponds to 1 mm.

Two cameras were set up to concurrently record the side and bottom views of the droplets upon deposition. The contact angles (θ) were measured by extracting and analyzing the side-view snapshots for the first and last 10 seconds of a 100 s acquisition period using a Matlab code base on tangential angle. Through the bottom-view snapshots, the wetting states of the droplets were determined.

3.3 Results and Discussion

The side and bottom-views of water droplets resting on two superhydrophobic substrates of different solid fractions (S1, S2) in CB state are presented in Fig. 3.2a and b, respectively. Figure 3.2c, on the other hand, shows the side and bottom view of a droplet in W state on S2 surface. Note the change in contrast comparing Fig. 3.2b with c.

The side and bottom-view representative snapshots of droplets resting on S1 and S2 surfaces containing different concentrations of SDS are presented in Fig. 3.3. It can be noticed that, the droplets with SDS concentrations ranging from 0 to 0.5 CMC are in CB state on S1 surface and in W state for 0.75 and 1 CMC, Fig. 3.3. The droplets on S2 surface, however, show a metastable behavior. For concentrations ranging from 0 to 0.75 CMC both CB and W states occurred upon deposition, while all 1 CMC droplets demonstrated Wenzel state, see Fig. 3.3b and c.

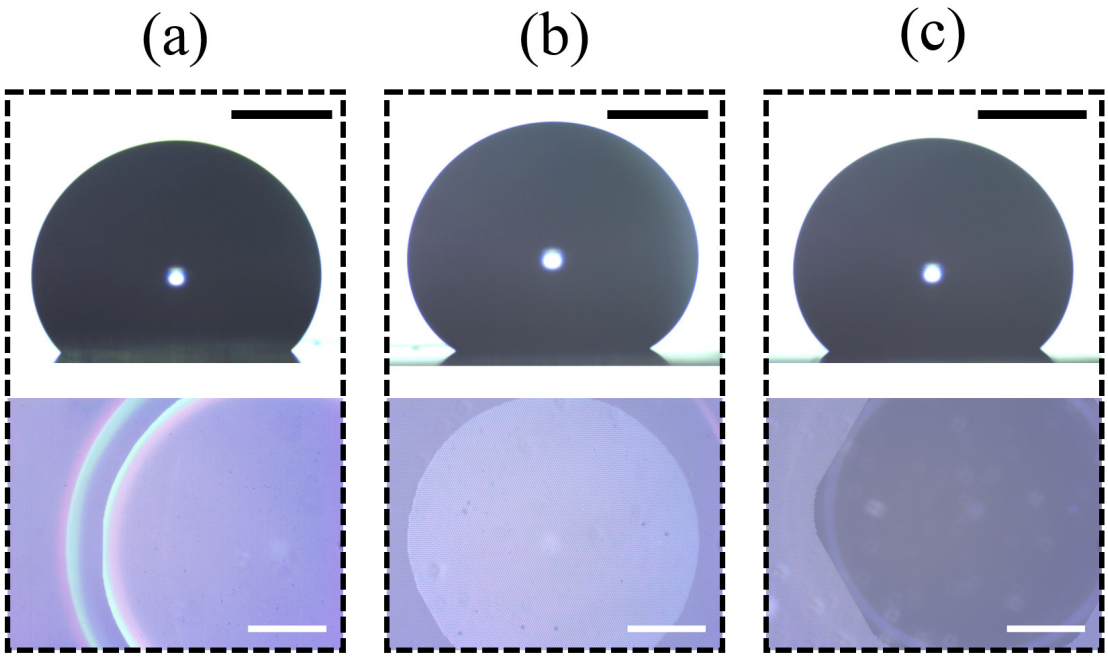

Figure 3.2: (a) Side and bottom views of a water droplet resting on S1 surface (r=2.608, Φ=0.466) in CB state. (b) and (c) Side and bottom views of a water droplet resting on S2 surface (r=1.480, Φ=0.138) in CB state and in W state, respectively. Scale bars for side and bottom views correspond to 1 mm and 500 μm, respectively.

The number of occurrence of each state for 7 to 9 trials at each concentration is presented in Fig. 3.4. It can be observed that the occurrence of Wenzel state is higher at concentrations above 0.25 CMC, whereas the CB state is more probable to happen at concentrations below 0.25 CMC, except for water.

It is worth to emphasize that the occurrence analysis is not provided for S1 surface, as the droplets at different concentrations experienced a single state (only CB or W) upon deposition on this surface for all trials. Such distinct wetting behaviors can be attributed to the higher roughness and solid fraction of S1. Based on the a previous study [65], a 10 μl water droplet deposited on surface S1, with the geometrical properties presented in Table 3.1, is likely to be in a stable Cassie-Baxter state. While on S2 surface, the droplet is anticipated to be in a Wenzel state. From such analysis it can be deduced that, the CB droplets on S2 surface are in a metastable state.

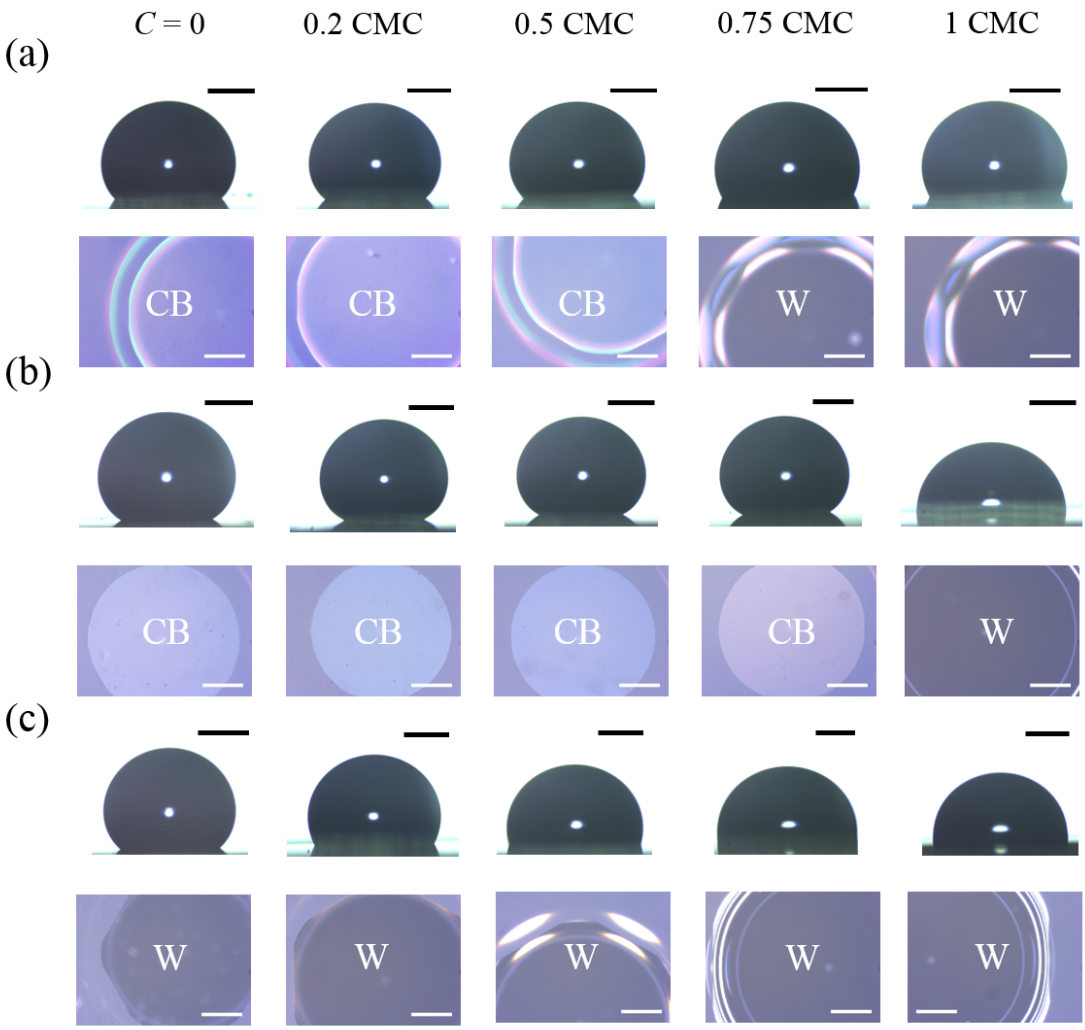

Figure 3.3: Influence of SDS concentration, roughness and solid fraction on wetting states. Side and bottom views of aqueous droplets laden with different concentrations of SDS (0 to 1 CMC) resting on (a) S1 surface (r=2.608, Φ=0.466) and (b) S2 surface (r=1.480, Φ=0.138), transiting from CB to W state. (c) Side and bottom views of droplets laden with SDS from 0 to 1 CMC resting on S2 surface always in W state. Scale bars for side and bottom views correspond to 1 mm and 500 μm, respectively.

Detailed contact angle data evaluated over a 100 s time period, for the complete range of SDS concentrations for all trials is presented in Fig. 3.5 to 3.14 for S1 and S2 surfaces.

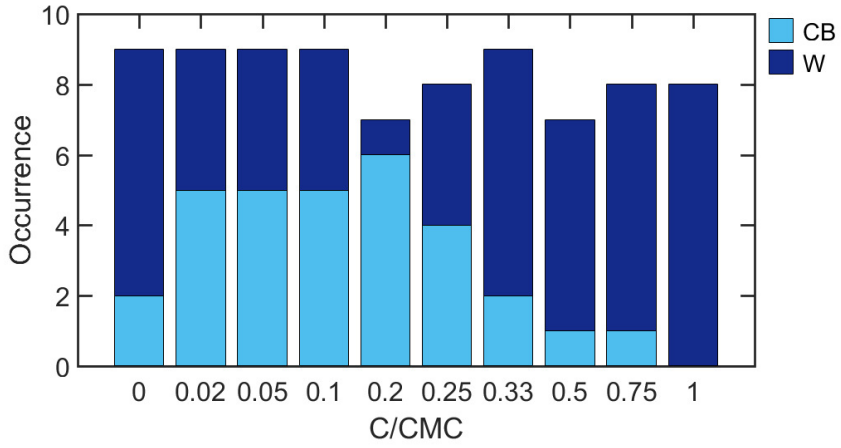

Figure 3.4: Occurrence of Cassie-Baxter or Wenzel states on S2 surface for different concentrations.

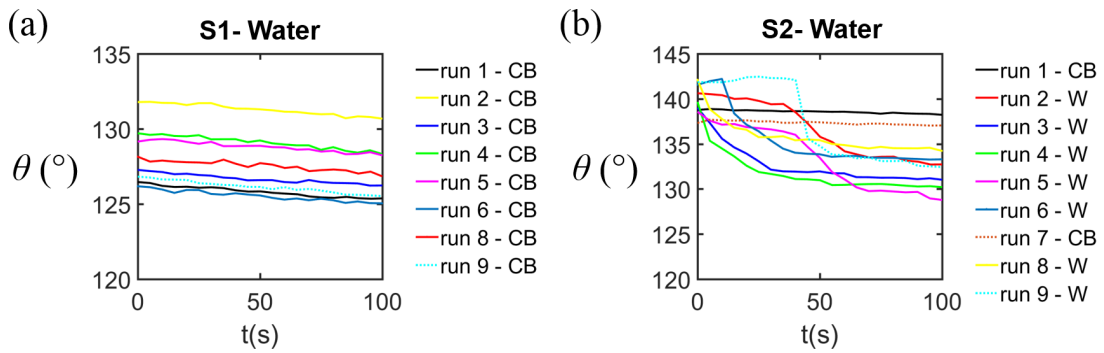

Figure 3.5: Detailed contact angle data for water on (a) S1 and (b) S2 surfaces during a 100 s time period.

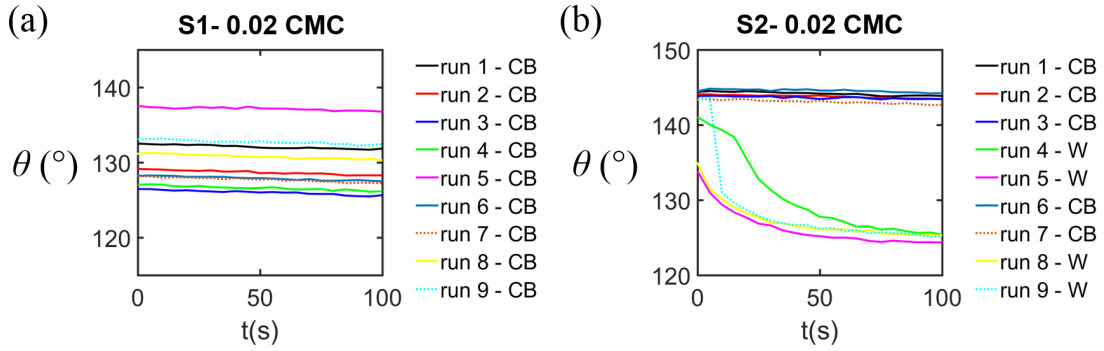

Figure 3.6: Detailed contact angle data for 0.02 CMC experiments on (a) S1 and (b) S2 surfaces during a 100 s time period.

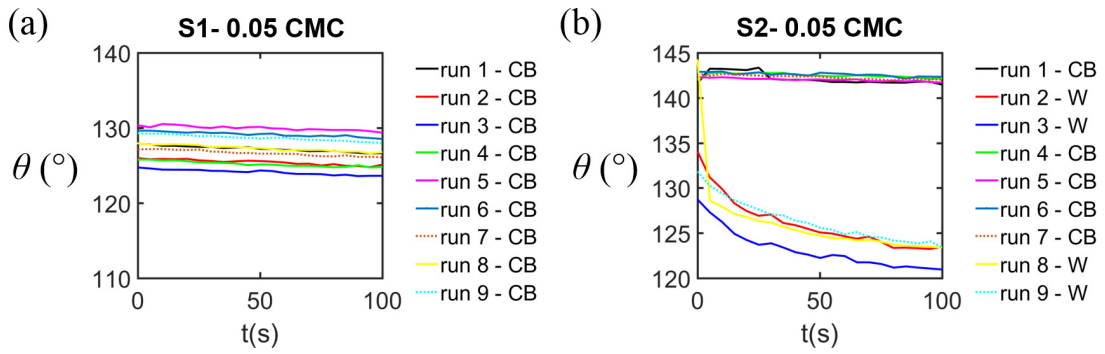

Figure 3.7: Detailed contact angle data for 0.05 CMC experiments on (a) S1 and (b) S2 surfaces during a 100 s time period.

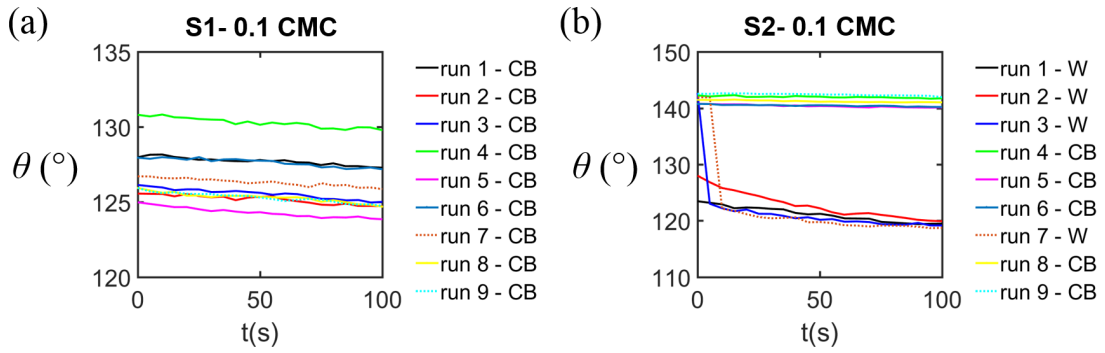

Figure 3.8: Detailed contact angle data for 0.1 CMC experiments on (a) S1 and (b) S2 surfaces during a 100 s time period.

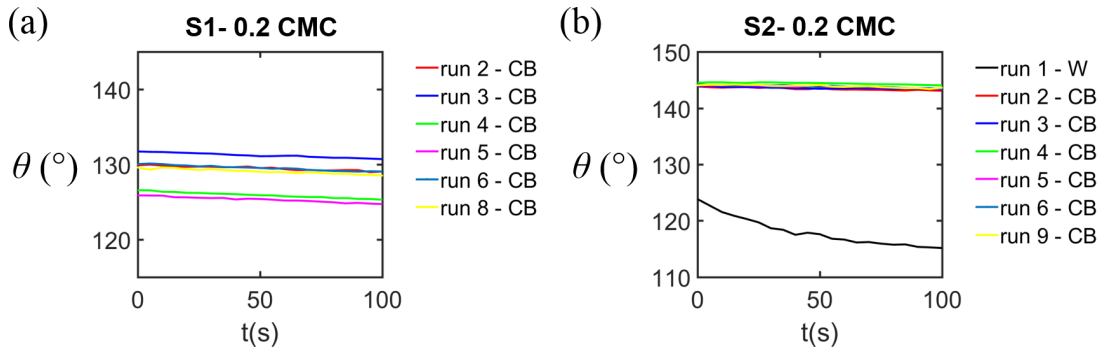

Figure 3.9: Detailed contact angle data for 0.2 CMC experiments on (a) S1 and (b) S2 surfaces during a 100 s time period.

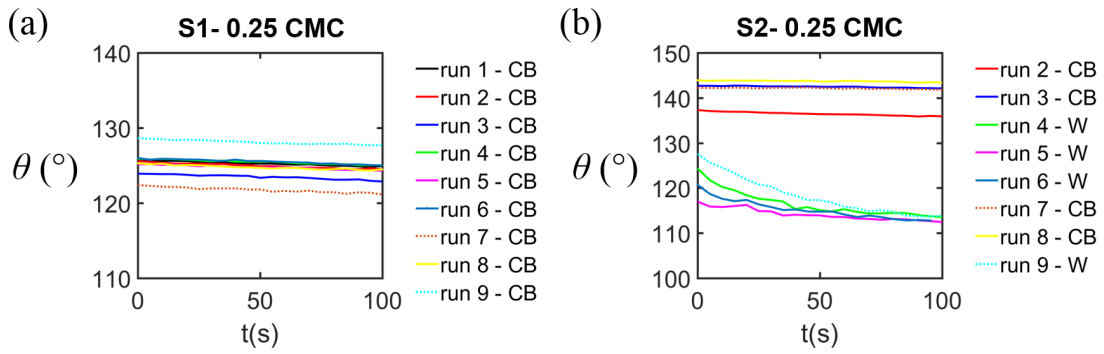

Figure 3.10: Detailed contact angle data for 0.25 CMC experiments on (a) S1 and (b) S2 surfaces during a 100 s time period.

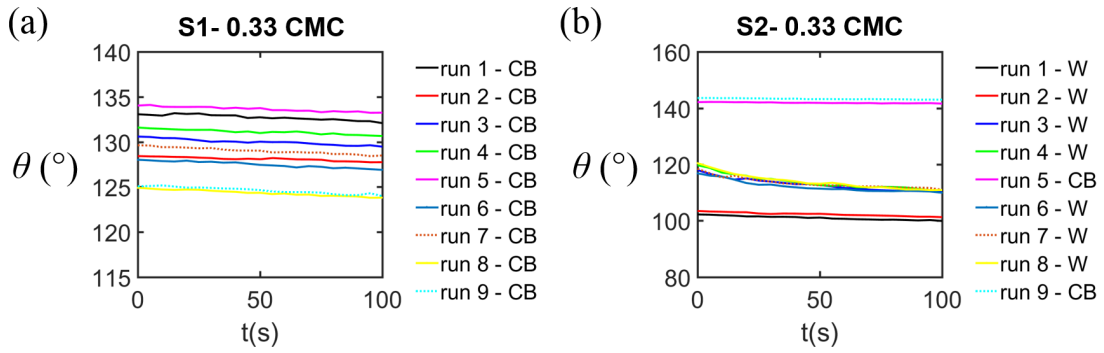

Figure 3.11: Detailed contact angle data for 0.33 CMC experiments on (a) S1 and (b) S2 surfaces during a 100 s time period.

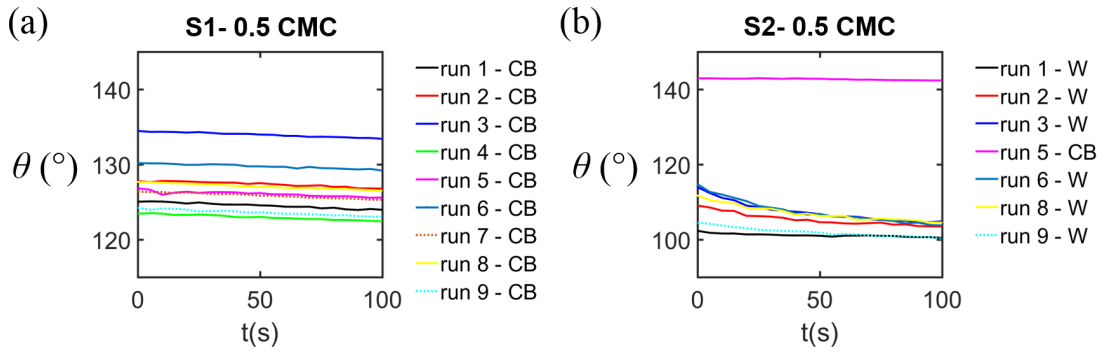

Figure 3.12: Detailed contact angle data for 0.5 CMC experiments on (a) S1 and (b) S2 surfaces during a 100 s time period.

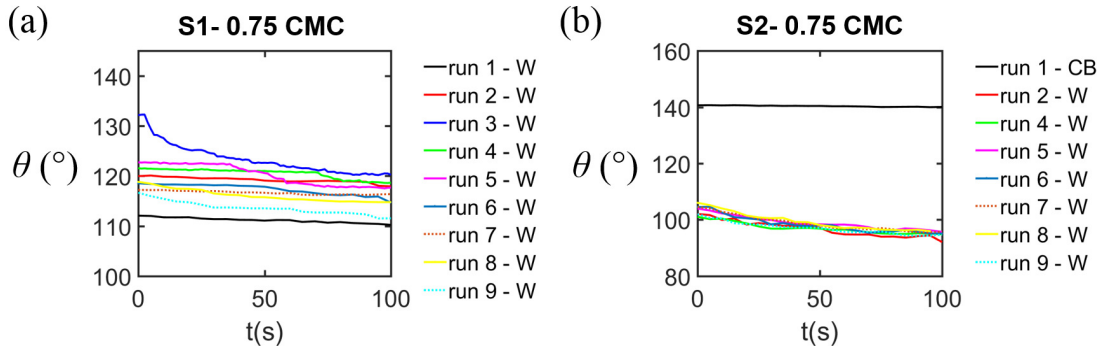

Figure 3.13: Detailed contact angle data for 0.75 CMC experiments on (a) S1 and (b) S2 surfaces during a 100 s time period.

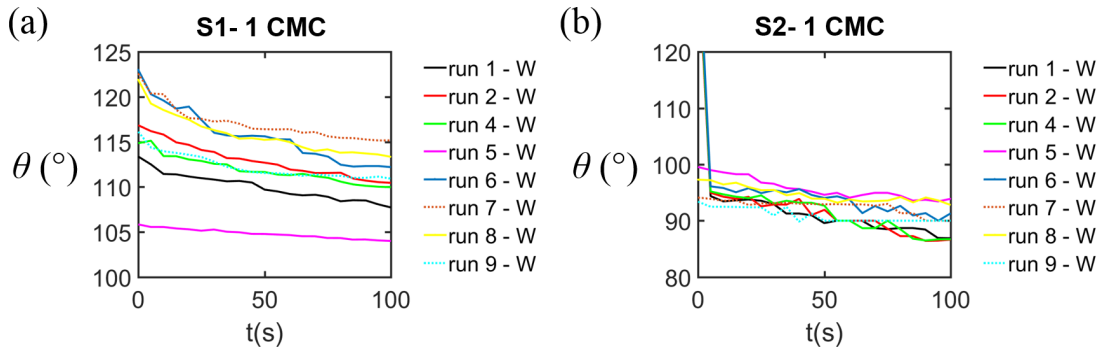

Figure 3.14: Detailed contact angle data for 1 CMC experiments on (a) S1 and (b) S2 surfaces during a 100 s time period.

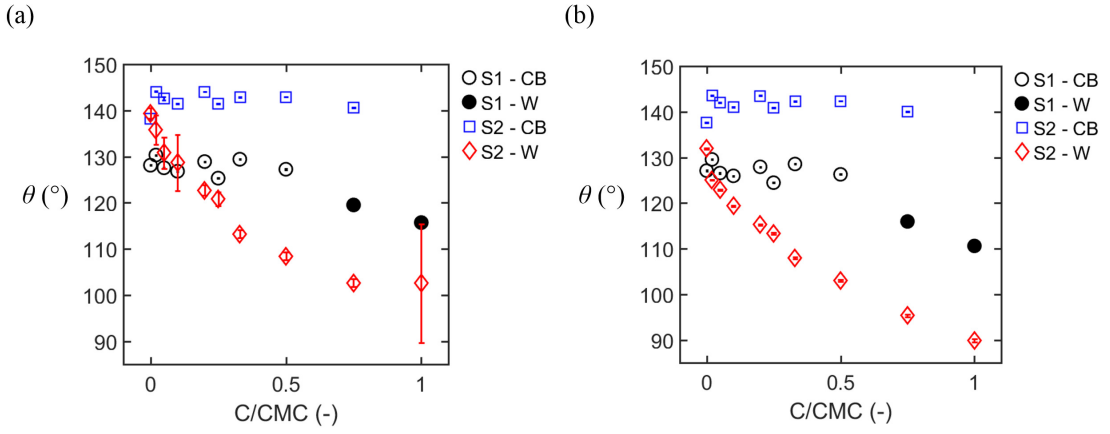

Figure 3.15: Average contact angle measured for the entire range of SDS concentrations (0 to 1 CMC) on S1 and S2 surfaces for CB and W wetting states during (a) the first 10 s and (b) the last 10 s of a 100 s period.

The contact angle behavior with SDS concentration averaged over the first and last 10 s of a 100 s time period is shown in Fig. 3.15a and b, respectively. Considering the droplets in CB state, the contact angle on S2 surface is in overall higher than that on S1 surface. The standard deviations (σ_θ) in this figure are evaluated based on equation (3.1),

$$\sigma_\theta = \sqrt{\frac{1}{N-1}\sum_{i=1}^{N}(\theta_i - \theta)^2}, \tag{3.1}$$

where i is the run number (1 to N), θ_i is the contact angle measured in i^{th} run, and θ is the average contact angle.

The contact angle of droplets in CB state (whether on S2 or S1 surface) is found to be almost constant with SDS concentration. The droplets resting on S1 surface were on CB state for concentrations equal and less than 0.5 CMC, and experienced a W state for concentrations above that. For droplets deposited on S2 surface, 1 CMC was the only concentration at which CB state was not evidenced. As stated earlier the droplets on S2 surface are, nevertheless, in a metastable state for concentrations other than 1 CMC. In other words, the droplets may experience a CB or a W state, whereas the droplets on S1 face a single wetting state at each concentration (either CB or W). The contact angle of the droplets in W state progressively decreases with SDS concentration. For instance, by increasing the SDS concentration from 0 to 1 CMC the contact angle of droplets resting on S2 surface in Wenzel state experiences a decrease of up to 30%.

3.4 Conclusion

The contact angle and wetting states of aqueous solutions of SDS were analyzed on two superhydrophobic surfaces with moderate (S2) and high (S1) roughness levels. It was noticed that by increasing the concentration of SDS it is more probable to obtain a Wenzel wetting state. The droplets deposited on S1 (r=2.608, Φ=0.466) were on stable Cassie-Baxter state for concentrations up to 0.5 CMC and were on Wenzel state for 0.75 and 1 CMC. On S2 surface (r=1.480, Φ=0.138), the droplets experienced a metastable state for concentrations

up to 0.75 CMC, as both states were likely to happen upon deposition. On both surfaces, the contact angle of droplets in CB state demonstrated a weak dependence on surfactant concentration. On the contrary, the contact angle of droplets in Wenzel state decreased noticeably with concentration.

Chapter 4

Wetting and evaporation of nanofluids on superhydrophobic surfaces[1]

4.1 Introduction

A significant step toward effective use of nano-materials in a variety of applications, such as flexible electronics [83], optical [84], thermal [85, 86] and nanofluidic devices [87], is the fabrication of robust nanostructures. Photonic crystals, in particular, have attracted a great deal of attention due to their ability to control and guide photons in a manner analogous to the capability of electronic crystals to manipulate electrons. Photonic crystals can be manufactured using top-down and bottom-up methods in two (2D) and three (3D) dimensions [88]. Top-down approaches consist of lithography with ions, atoms, electrons, and photons. Bottom-up techniques consist of particle assembly driven by gravitational [89], electric [90] and magnetic fields [91], as well as assembly through (solvent) evaporation [92].

[1]The material presented in this chapter is based on Bigdeli, M.B. and Tsai, P.A., "Making photonic crystals via evaporation of nanoparticle-laden droplets on superhydrophobic surfaces", submitted to Scientific Reports, 2017.

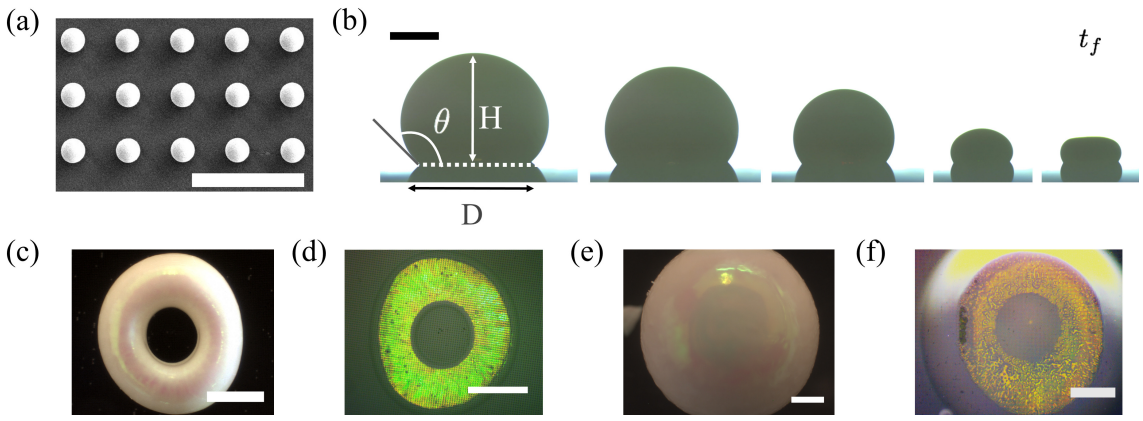

Figure 4.1: (a) Scanning electron microscopy (SEM) image of the top-view superhydrophobic surface used. Scale bar corresponds to 30 μm. (b) Side-view snapshots of an evaporating droplet containing 5wt% silica nanoparticles on superhydrophobic substrate. The scale bar in (b) corresponds to 1 mm, and the time-scale of complete drying, t_f = 4770 s. Optical microscope images of fabricated photonic crystals in (c) to (f). (c) top-view and (d) bottom-view images of the toroidal deposit pattern corresponding to water droplets laden with low concentration ($\approx$ 5wt%) of NPs. (e) top-view and (f) bottom-view images of the spherical deposit pattern resulting from evaporation of high concentration ($60 \pm 5 wt\%$) colloidal drops. Scale bars in (c) to (f) are 500 μm.

Bottom-up assembly techniques are increasingly preferred, on account of the ease of process, the lower cost, and the production potential at an industrial scale [93]. Among bottom-up methods, using the evaporative self-assembly mechanism is a well established technique for the fabrication of 2D photonic crystals. However, the complex nature of the self-assembly methods introduced for creating 3D photonic crystals, including acoustic levitation [94], inkjet printing [95] and solvent extraction [96], suggests that there is room for further development. Superhydrophobic surfaces have been intensively studied in recent decades, owing to their non-sticking and self-cleaning properties [68, 72, 97]. Primarily researchers have been interested in their fabrication and wetting transition [98, 99]. Relatively few studies (albeit with an increasing number) have focused on 3D depositions of various materials through evaporative self-assembly on superhydrophobic surfaces. Some examples include drying droplets of protein (lysozyme) solution [100], suspensions of micro-particles [101, 102], colloidal semiconductor (CdSe/CdS) nanorods [103], colloidal polymer dispersion [104], and suspension of ceramic (alumina) nanoparticles [105], on superhydrophobic sur-

faces. However, systematic investigations concerning the evaporation of colloidal droplets on superhydrophobic surfaces with the intention of making light diffracting 3D photonic crystals are still rare.

In this Letter, we have exploited the effect of particle concentration and have chosen a proper superhydrophobic substrate for the facile creation of 3D photonic crystals. Specifically, colloidal drops with two distinct initial concentrations were left on a superhydrophobic surface to evaporate at ambient conditions. Through this simplistic and reproducible technique we were able to fabricate 3D photonic crystals with two different morphologies: donut-shaped (toroidal) and quasi-spherical for the low and high particle concentrations, respectively. Furthermore, we have investigated the evaporation dynamics, the packing, and the reflection peaks of these self-assembled nanoparticles forming photonic crystals.

4.2 Experimental

The superhydrophobic substrates were fabricated through a replica molding process using Polydimethylsiloxane (PDMS). Substrates were transparent and consisted of parallel cylindrical pillars forming a square pattern of an area size about 2×2 cm^2 [18]. The scanning electron microscope (SEM) image of the superhydrophobic surface texture is shown in Fig. 4.1a. The contact angle of a water droplet of 10 μl volume on the superhydrophobic surface is $\approx 150^\circ$ ($\pm\ 4^\circ$). Silica nanoparticles (NPs) were dispersed in milli-Q water to form suspensions of 5 and 60 wt% weight fraction of NPs ($f_{w,p}$). The average size of nanoparticles, d_p, analyzed from SEM images is 252 nm, while the manufacture data provided is d_p = 261 nm, with coefficient of variation of 6.4%.

Three cameras were simultaneously used to capture the side, bottom, and top views of the evaporating droplets. The side view was used to measure the droplet contact angle (θ), base diameter (D), and height (H). Figure 4.1b provides representative snapshots of an evaporating water droplet laden with 5 wt% nanoparticles on the superhydrophobic substrate. Through top and bottom views, we investigate and analyze the symmetry of the droplet shape, onset of donut formation, and the wetting transition from a partial wetting

Cassie-Baxter (CB)[3] to completely wetting Wenzel (W)[2] state [106, 65]. Snapshots of evaporating droplets were extracted and analyzed using a Matlab code. All experiments were conducted at room temperature, $25 \pm 1^{\circ}C$, and relative humidity of $18 \pm 2\%$.

The reproducibility of final deposit patterns was checked via conducting independent experiments for at least three times (for each particle concentrations). For instance, shown in Fig. 4.1c–f are the bottom and top views of the created photonic crystals in this study. Low concentration of NPs resulted in a donut-shaped structure (Fig. 4.1c,d) whereas at high concentrations, particles form a spherical structure with a cavity (also known as vacuole[107]) beneath, see Fig. 4.1e,f.

4.3 Results and Discussion

Figure 4.2a–e shows the detailed evaporation dynamics of nanoparticle-laden droplets, namely the time evolution of the droplet base diameter, height, contact angle and shape. The droplet diameter for both concentrations was initially pinned and subsequently receded as the droplets dried out, as shown by the diameter plot in Fig. 4.2a,. At the next stage of evaporation, droplets with 60 wt% of NPs underwent a sudden increase in base diameter (marked by a vertical red arrow), due to the formation of the vacuole beneath the droplet. This was followed by a slight decrease until the contact line was pinned once again until completely dry. On the other hand, low concentration droplets (5 wt%) were pinned after the latter receding regime until the end of the process.

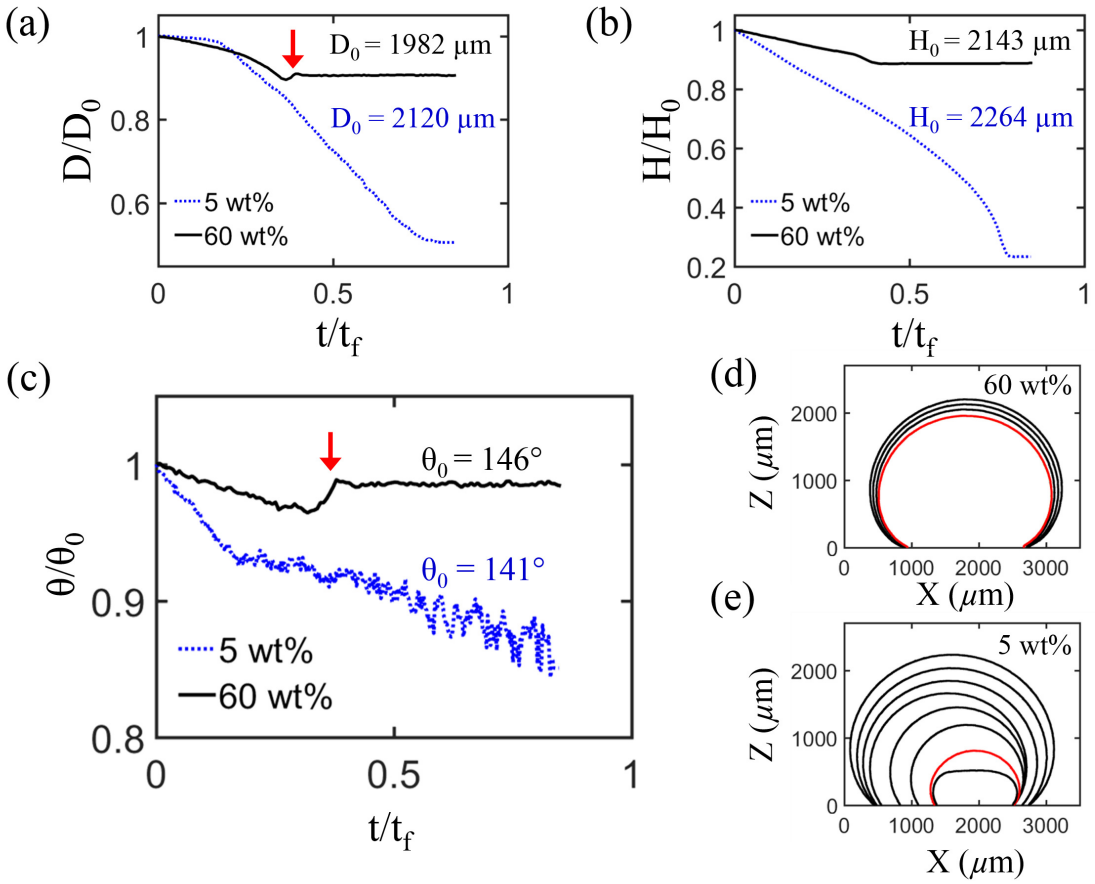

Figure 4.2: Evolution of normalized base diameter in (a), height in (b), and the tangential contact angle in (c) of evaporating droplets containing $f_{w,p}$ = 5 wt% and 60 wt% of nanoparticles on the superhydrophobic surface (measured every 10 s). Here D_0, H_0, and θ_0 are the initial droplet diameter, height, and tangent contact angle (at t=0), respectively. The averaged final evaporation time (t_f) for 5wt% and 60wt% experiments are 4668 s and 1485 s, respectively. (d) and (e) Side-view evolutions of evaporating droplets for 60 wt% and 5 wt% of NPs, respectively. Red lines denote the onset of second pinning before complete desiccation.

The droplet height decreased continuously for both concentrations, as revealed in Fig. 4.2b. The temporal evolution of contact angles is depicted in Fig. 4.2c. The droplets were initially at Cassie-Baxter state, i.e. $\theta_0 \approx 141^\circ$ and $\approx 146^\circ$ for the 5wt% and 60wt% experiments, respectively. They maintained high contact angles ($\gtrsim 120^\circ$) during the entire evaporation process. Similar to the base diameter, 60 wt% droplets underwent a jump in the contact angle due to the growth of a cavity below the droplet. The evolution of the shape of the droplets during evaporation was extracted through image analysis of the side-view snapshots (usually captured at 0.5 fps), as in Fig. 4.2d and e. Red lines highlight the point where the droplets began to pin before complete evaporation.

To further analyze the 60 wt% experiments resulting in quasi-spherical configurations, the deposits were detached from the superhydrophobic substrate and placed upside down in a SEM device. Figure 4.3a shows that a vacuole formed at the bottom of the deposit. The higher magnification SEM images in Fig. 4.3b and c, reveal the footprints of pillars in the flat region around the cavity. The deposited particles apparently stayed on top of the pillars and did not penetrate inside the microstructures, this suggests that this area of the droplet stayed at a partially wetting status during the entire evaporation process. However, from the bottom view of the 60 wt% droplets, we could see that the central region of the droplet, forming a dome shaped cavity later on, wet the substrate right before complete dryout.

Similar observations have been also reported in a few studies concerning drying of nanoparticle-laden droplets on superhydrophobic surfaces. Pauchard and Couder [104], investigated the evaporation of dilute (volume fraction of particles ($f_{v,p}$) = 15%) and concentrated ($f_{v,p}$ = 40%) droplets laden with latex particles resting on a superhydrophobic surface. They observed toroidal- and spheroidal-shaped deposits with a cavity underneath for dilute and concentrated droplets, respectively. Accardo et al. [100] studied the evaporation of droplets laden with lysozyme on patterned superhydrophobic surfaces of poly(methyl methacrylate) (PMMA) at room temperature. A hollow sphere was observed from the optical microscopy image of the deposit formed on the substrate. Chen and Evans [105],

explored the desiccation of aqueous droplets laden with alumina nanoparticles on a superhydrophobic surface for different initial concentrations. They observed that in dilute experiments ($f_{v,p}$ = 5.7%) the droplet flattened and left a concave shape on top. In the case of the concentrated droplets ($f_{v,p}$ = 26%), a vacuole was evidenced beneath the deposit. However, these experimental studies did not focus on the fabrication of 3D photonic crystals.

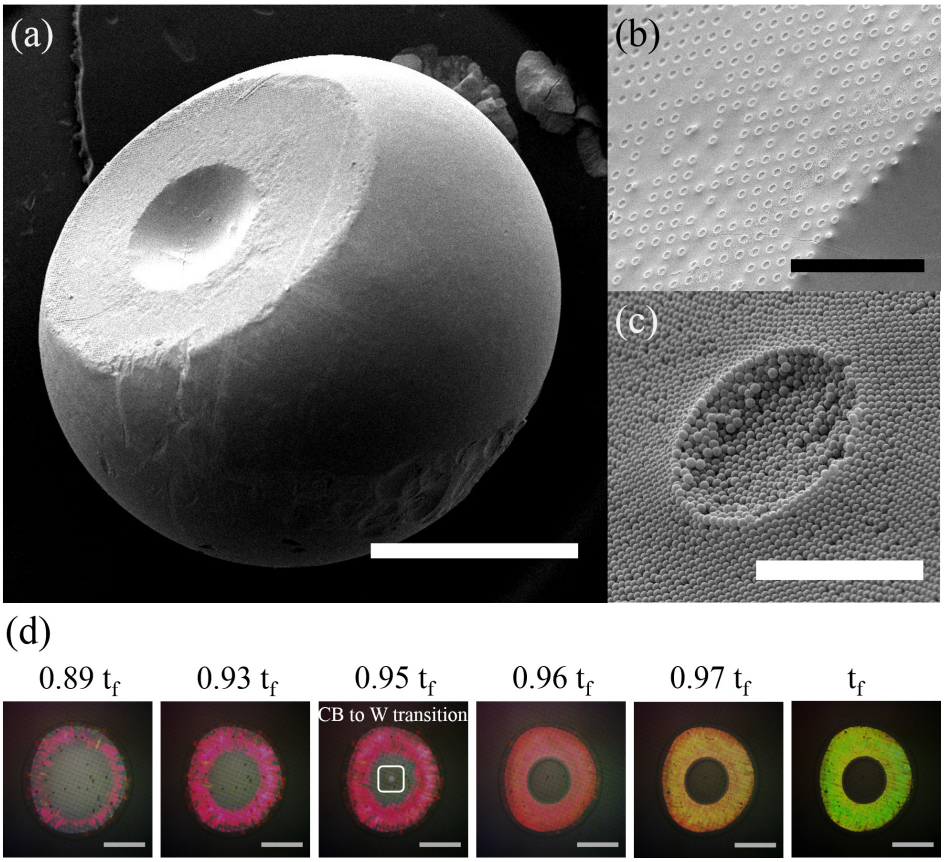

Figure 4.3: SEM images of the bottom of a dried NP-laden drop ($60 \pm 5wt\%$) with different magnifications: (a) 40x, entire deposit; (b) 600x, pillars footprint in the flat region around vacuole; and (c) 10000x, footprint of a single pillar. Scale bars equal to 1000, 100 and 5 μm in (a), (b) and (c), respectively. (d) Optical microscope snapshots (bottom view) of colloidal drop containing 5 wt% of 261 nm silica NPs at room temperature near the end of evaporation process (i.e. from $0.89t_f$ to t_f). At t = 0.95 t_f the drop undergoes Cassie to Wenzel transition. Scale bars in (d) correspond to 500 μm and t_f = 4770 s.

To gain more insights into the droplet behavior throughout evaporation, the bottom

view images were studied. Figure 4.3d presents the bottom view snapshots of an evaporating 5wt% droplet in the later stage of evaporation process, i.e. during the second pinning event. The droplet maintained a constant contact area starting from 0.89 t_f (until complete desiccation), transited to Wenzel state at 0.95 t_f, and eventually dried out. During evaporation, as the silica NPs organize themselves, the color of the contact area gradually changes from white to red, orange, yellow and finally green. This color sequence is due to the reflected light scattered by the self-organized NPs, which depends on the drying stage and process (discussed detailed below).

The SEM images of both top and bottom views of 60wt% deposits, provided in Fig. 4.4a, reveal that the particles were organized in a hexagonal pattern. More specifically, from Voronoi analysis over areas of ≈ 11 and ≈ 8 μm^2 for top and bottom views, respectively, 70% and 76% of NPs have 6 close neighbouring particles. Hence, most of the particles were packed in a hexagonal pattern. The latter hexagonal arrangement can be attributed to either a {111} plane of a face-centred cubic (fcc) system or a {001} plane of a hexagonal closed packed (hcp) system. Despite this, it has been shown through microscopic characterization of nanosized silica spheres [108] in addition to the free energy calculations [109], that the fcc close packing can be favored over the hcp.

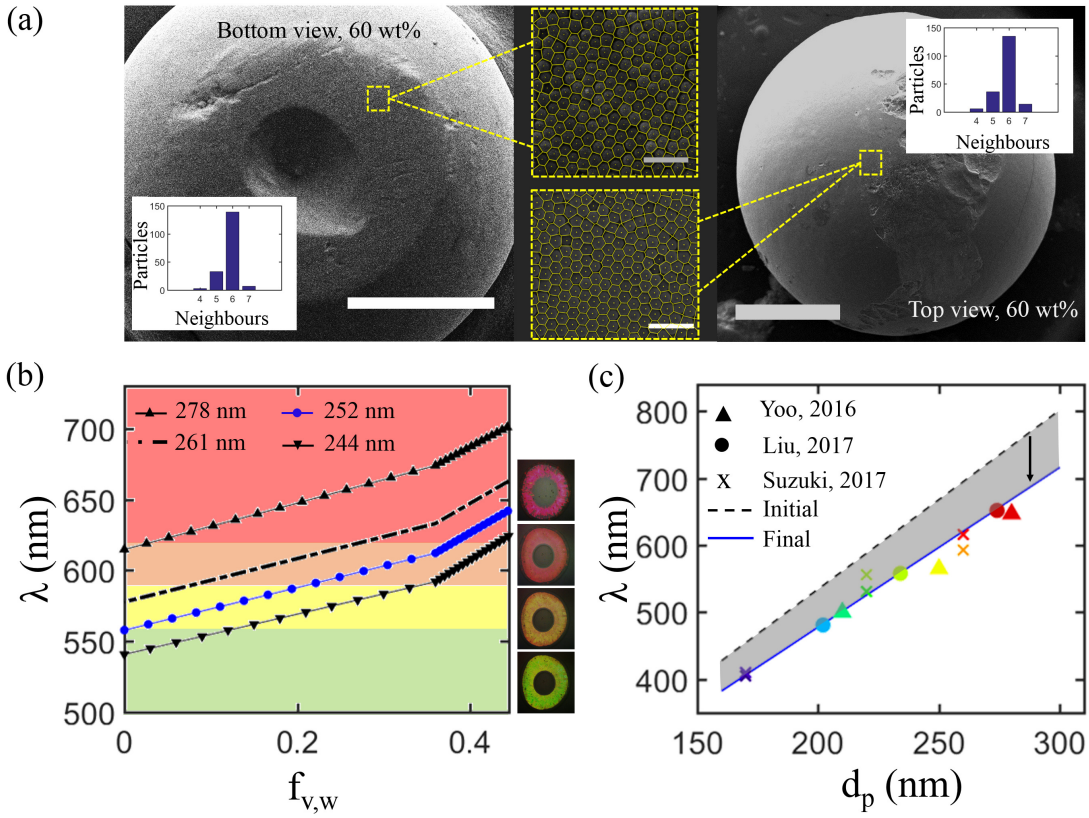

Figure 4.4: (a) Top and bottom view SEM image of self-assembled silica particles, forming a top-spherical deposit with a cavity underneath on superhydrophobic surface after evaporation. Yellow dashed squares depict the Voronoi analysis of the packing of nanoparticles based on the image acquired from high magnification SEM. Bar diagrams reveal the number of close neighbors each particles have in the region under study (dashed square). Zoomed out scale bars equal 800 μm; Scale bars in insets equal 1 μm. (b) Analysis of the reflected colors from the bottom view of an evaporating droplet using Bragg-Snell equation. (c) Prediction by our current model on the reflected wavelengths compared with existing experimental data [110, 111, 112] (obtained from the bottom-view of a desiccating polystyrene colloidal droplet).

The change in the bottom view color during evaporation can be explained based on the combined Bragg-Snell laws [113] for a {111} plane of a fcc structure

$$\lambda_{max} = 2d_{\{111\}}n_{eff}, \tag{4.1}$$

where λ_{max} is the wavelength of the main reflectance peak, $d_{\{111\}}$ is the distance between {111} planes and equal to $\sqrt{\frac{2}{3}}D$, with $D = d_p + \epsilon$ being the center-to-center distance between spherical particles of diameter d_p, and surface-to-surface distance of ϵ. For more information see supporting material. Furthermore, n_{eff} is the effective refractive index, which for a medium made of silica particles (p), water (w) and air (a) can be approximated by

$$n_{eff} = \sqrt{f_{v,p}n_p^2 + f_{v,w}n_w^2 + f_{v,a}n_a^2 - sin^2(\alpha)}, \tag{4.2}$$

where n and f_v correspond to refractive index and volume fraction of each components, respectively. α is the angle of incidence, which is 0° for the normal incident.

During evaporation, the particles tend to organize themselves in a fcc type lattice [108]. The space between particles is initially filled with water having thickness of ϵ on the diagonal (see Fig. S1 in Supplementary Info), as an initial stage (1), and subsequently both air and water occupy the space as evaporation goes on, in stage (2). In other words, stage (1) corresponds to the range where the particle volume fraction varies from the melting volume fraction ($f_{v,p}$ = 0.545) to the random close packing limit, where $f_{v,p}$ = 0.64. It is assumed that there are only water and silica particles inside the system at the stage (1) ($f_{v,a}$ = 0). During the stage (2), as the volume fraction of water diminishes due to evaporation, volume fraction of particles and air increase. This stage is completed once the maximum cubic close packing limit, where $f_{v,p}$ = 0.74, is reached. The results of the optimal reflected colour based on this model are presented in Fig. 4.4b. See Supplementary Material for the detailed analysis.

Based on the coefficient of variation provided by the manufacturing company (6.4%), the reflectance peaks were calculated for three particle sizes, namely, 244 nm, 261 nm (mean diameter) and 278 nm. The reflectance peaks were also evaluated for the average particle size (252 nm), analyzed using SEM images of self-assembly nanoparticles, such as the insert in Fig. 4.4a. As revealed in Fig. 4.4b, larger particles result in reflection of longer

wavelengths. More specifically, for nanoparticles of d_p =278 nm, the wavelength varied from red to orange. For 261 nm particles, the color shifted from red to yellow, while 244 nm NPs covered the orange to green wavelength region. In this analysis, the reflectance peaks varied from red to green for average particle size of 252 nm, which agree well with our experimental data shown in Fig. 4.3d.

We further extended our analysis to drying colloidal suspensions for different sizes and materials found from the literature. In Fig. 4.4c, we predicted the sequential variation of the reflected wavelength from the bottom view during evaporation (grey area) for polystyrene particles (n_p = 1.59) of varying diameters (170 to 340 nm). The top dashed line corresponds to the reflected wavelength at the beginning of stage (1), while the lower solid line is the wavelength reflected at the end of stage (2), when the deposit was completely dried out. The vertical downward arrow depicts the variation in the wavelength of a typical droplet during desiccation. Moreover, our analyses show good agreement with existing experimental work [112, 111, 110]. The different symbol colours represent the final reflectance wavelength obtained by the corresponding materials.

4.4 Conclusion

We have successfully fabricated 3D photonic crystals of different sizes and shapes using evaporation-driven self-assembly of nanoparticles on a superhydrophobic surface. Toroidal and spherical shaped crystals have been created by aqueous droplets suspended with 5 wt% and to 60 wt% of NPs, respectively. The high-resolution snapshots captured from simultaneous top, bottom, and side views show distinct evaporating processes for different nanoparticle concentrations. The nanofluid droplets with 60 wt% nanoparticles maintained a large contact angle with a pinned contact line from the early drying stage, but a decreasing contact angle, droplet diameter, and height for droplets laden with 5 wt% nanoparticles. In addition, scanning electron microscopy images of the crystal structures proved that particles organized themselves into hexagonal patterns. From the bottom view evolution of the droplets, a change in color from red to green was observed for both NP concentra-

tions. A model considering the particle diameter, material, interplanar distance, and the particle-water-air content of the droplet was developed to predict the color sequence during evaporation. The predictions agree well with our data for silica NPs and other experimental results with polystyrene NPs. The model can be further utilized effectively to predict the reflected light/color by photonic crystals fabricated and self-assembled via simple evaporation.

Chapter 5

Conclusions and Outlook

In this thesis, the wetting and evaporation of simple and complex fluids have been investigated on superhydrophobic surfaces of a variety of geometric arrangements and structures.

Through experiments on wetting and evaporation of pure water droplets on superhydrophobic nanostructures of different roughness levels, three distinct wetting behaviors was evidenced:(1) A Cassie-Baxter wetting state was formed on surfaces with high roughness values. (2) A Wenzel wetting state was formed on surfaces with moderate roughness levels. (3) Droplets deposited on surfaces with low roughness levels, demonstrated a metastable behavior. The evaporation experiments on superhydrophobic nanostructures revealed evaporation behavior similar to that of microstructured and flat hydrophobic surfaces, consisting of a constant contact radius regime, follow by a constant contact angle trend, and eventually a mixed mode.

Experiments with aqueous surfactant solutions (0 to 1 CMC) on superhydrophobic microstructures with moderate and high roughness degrees have been conducted. On the surface characterized with high roughness level, the droplets were in Cassie-Baxter state for concentrations of up to 0.5 CMC, while they formed a Wenzel wetting state for higher surfactant concentrations. In contrast, on the surface characterized with moderate roughness level, the droplets displayed a metastable behavior for concentrations up to 0.75 CMC. The droplets formed a Wenzel state at 1 CMC surfactant concentration. The contact an-

gle of droplets in Cassie-Baxter state, on both surfaces, showed a weak dependence on concentration. This may be explained by partial air-liquid contact area of the drops in Cassie-Baxter state. Whereas, the contact angle of drops in Wenzel state demonstrated a strong concentration dependence.

For future investigation, it is very interesting to develop a theory explaining the contact angle and wetting behavior with respect to surfactant concentration. Additionally, the critical concentration after which the wetting state is switching can be investigated.

Based on evaporation experiments of nanoparticle-laden droplets on a superhydrophobic surface, structural photonic crystals can be fabricated. Crystals with toroidal and spheroidal structures were synthesized through evaporation of droplets laden with 5wt% and 60 wt% of nanoparticles, respectively. Using bottom view visualization, a change in color from red to green was observed during evaporation. Scanning electron microscopy images of the final crystal, revealed a closely packed hexagonal arrangement of nanoparticles. In addition, it was observed that a cavity formed beneath 60 wt% deposits. The light reflected from the structure was investigated through a Bragg-Snell analysis. Based on the latter analysis a model was developed to predict the colors reflected colors during evaporation for droplets laden with nanoparticles of different size and materials.

A possible extension of this work, could be experiments with nanoparticles of different sizes and materials and analysis of the reflected color from the resulting structures. Also, the structures may be cut using focused ion beam experiments to provide a direct experimental evidence on the lattice structure of the nanoparticles. Moreover, it is of interest to investigate the mechanism leading to the formation of a cavity beneath spheroidal deposits.

Appendix A

Structural packing of evaporation-driven self-assembly of nanoparticles

Figure A.1 demonstrates the arrangement of nanoparticles while approaching complete evaporation in a fcc lattice. Here, we have assumed that the thickness of the water layer around particles, denoted by $\epsilon(t)$, decreased linearly during evaporation from an initial value (ϵ_0) to 0. The latter initial value for each particle size was determined by finding the ϵ value corresponding to the melting volume fraction at stage (1). The ϵ_0 values for 244, 261 and 278 nm particles, were calculated to be 26, 28 and 30 nm, respectively. The lattice

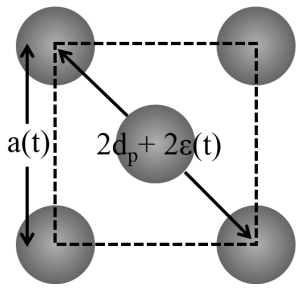

Figure A.1: Nanoparticle arrangement in a fcc lattice. As the thickness of the water layer around particles, denoted by $\epsilon(t)$, diminishes during evaporation, the lattice constant $a(t)$ decreases.

constant, evaluated by $a(t) = \sqrt{2}(d_p + \epsilon(t))$, and likewise the interplanar spacing, decrease accordingly. The interplanar spacing for cubic packing ($d_{\{hlk\}}$) can be calculated as follows:

$$d_{\{hlk\}} = \frac{a}{\sqrt{h^2 + l^2 + k^2}}, \tag{A.1}$$

where h,l,k are the Miller indices. As explained in the main body of the article, the hexagonal arrangement of the particles correspond to the {111} plane of the fcc lattice. Therefore, the interplanar spacing $d_{\{111\}}$ is evaluated by $\sqrt{\frac{2}{3}}(d_p + \epsilon)$.

To implement this model, two drying stages have been considered. The first one, being the change of particle volume fraction from $f_{v,p} = 0.545$, to the random close packing limit, where the volume fraction of air, is considered negligible. Assuming that the particles keep the same fcc arrangement, ϵ value corresponding to the random close packing limit was calculated. For example, for d_p=261 nm, the water layer thickness at a random close packing state was evaluated to be 13 nm. Hence, in the first stage, ϵ varies from 28 nm to 13 nm.

The second stage included a further increase of $f_{v,p}$ from the random to the cubic close packing limit. At this stage, $f_{v,a}$ was no longer considered negligible. The following relation holds for volume fractions in both stages:

$$f_{v,p} + f_{v,w} + f_{v,a} = 1 \tag{A.2}$$

Using this relation, the volume fractions for silica particles, water and air were computed. Subsequently, the effective refractive index of the composite medium was evaluated through equation (4.2) of the main text, for n_a=1, n_w=1.33 and n_p=1.46.
Eventually, having $d_{\{111\}}$ and n_{eff} values evaluated, equation (4.1) in the main text was implemented to calculate λ_{max}.

Two more larger areas of the bottom of the PhCs of 60 wt% suspensions are investigated in Fig. A.2 and A.3. The Voronoi analysis of two different regions covering areas of 45 and 48 μm^2 (i.e. 3 to 4 times the area considered before) shows that ≈78% and ≈73% of particles (481 out of 619 and 427 out of 588 particles, respectively) have 6 neighbouring particles.

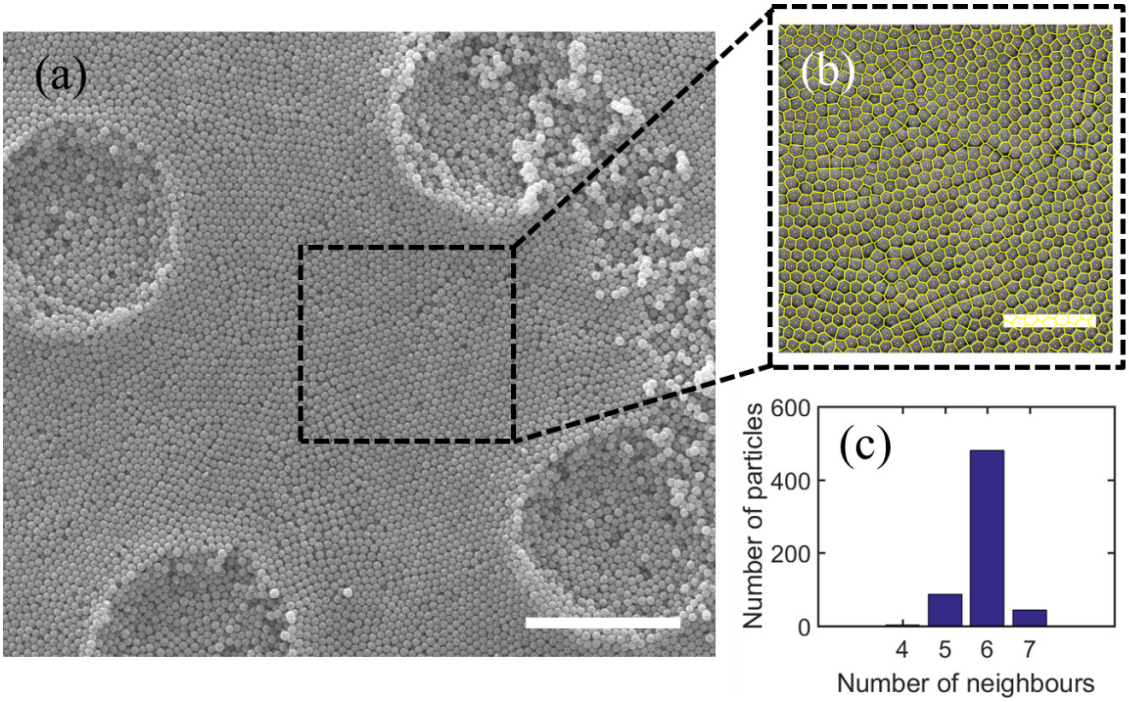

Figure A.2: (a) SEM image from the bottom of the deposit in the first region between 4 pillars. Scale bar corresponds to 5 μm (b) Voronoi analysis in an area of $\approx 45\mu m^2$. Scale bar corresponds to 2 μm (c) Bar diagram demonstrating 78% of particles have 6 neighbours.

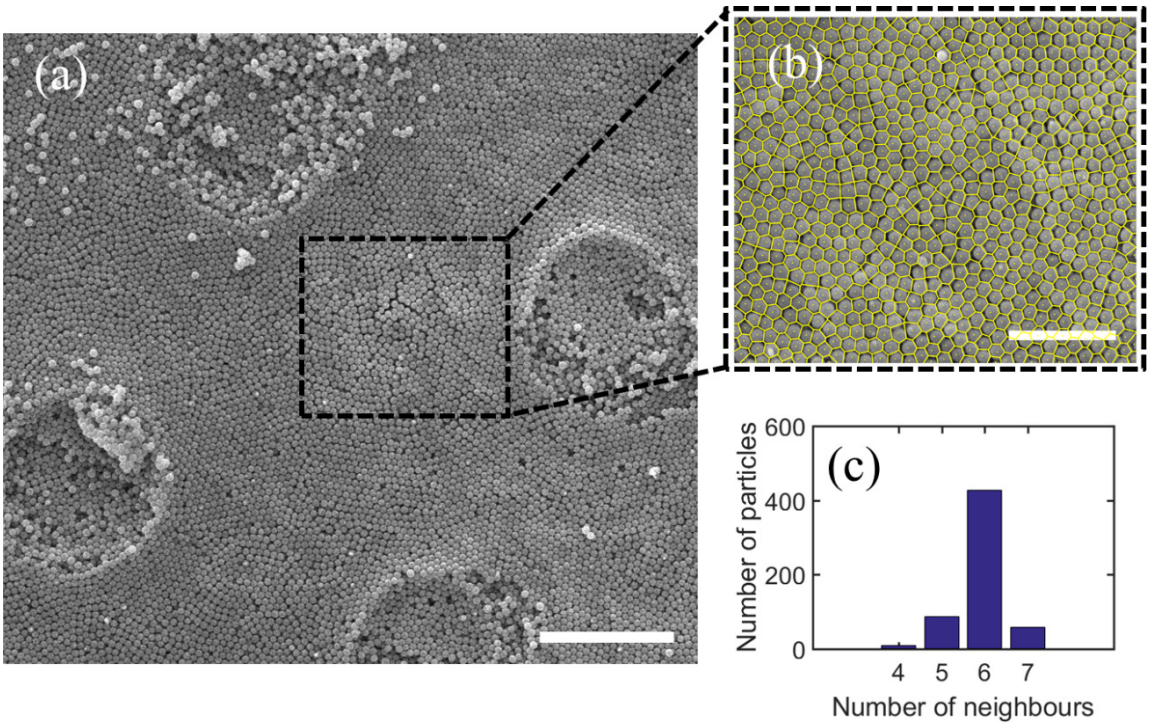

Figure A.3: (a) SEM image from the bottom of the deposit in the second region between 4 pillars. Scale bar corresponds to 5 μm. (b) Voronoi analysis in an area of $\approx 42\mu m^2$. Scale bar corresponds to 2 μm.(c) Bar diagram demonstrating 73% of particles have 6 neighbours.

References

[1] Thomas Young. An essay on the cohesion of fluids. *Philosophical Transactions of the Royal Society of London*, 95:65–87, 1805.

[2] Robert N Wenzel. Resistance of solid surfaces to wetting by water. *Ind. Eng. Chem.*, 28(8):988–994, 1936.

[3] ABD Cassie and S Baxter. Wettability of porous surfaces. *Trans. Faraday Soc.*, 40:546–551, 1944.

[4] Abraham Marmur. Wetting on hydrophobic rough surfaces: to be heterogeneous or not to be? *Langmuir*, 19(20):8343–8348, 2003.

[5] E Pierce, FJ Carmona, and A Amirfazli. Understanding of sliding and contact angle results in tilted plate experiments. *Colloids and Surfaces A: Physicochemical and Engineering Aspects*, 323(1):73–82, 2008.

[6] P Zhang and FY Lv. A review of the recent advances in superhydrophobic surfaces and the emerging energy-related applications. *Energy*, 82:1068–1087, 2015.

[7] RM Fillion, AR Riahi, and A Edrisy. A review of icing prevention in photovoltaic devices by surface engineering. *Renewable and Sustainable Energy Reviews*, 32:797–809, 2014.

[8] Richard Menini, Zahira Ghalmi, and Masoud Farzaneh. Highly resistant icephobic coatings on aluminum alloys. *Cold Regions Science and Technology*, 65(1):65–69, 2011.

[9] Guy Fortin. Super-hydrophobic coatings as a part of the aircraft ice protection system. In *AeroTech Congress & Exhibition*. SAE International, sep 2017.

[10] A Bisetto, D Torresin, MK Tiwari, D Del Col, and D Poulikakos. Dropwise condensation on superhydrophobic nanostructured surfaces: literature review and experimental analysis. In *Journal of Physics: Conference Series*, volume 501, page 012028. IOP Publishing, 2014.

[11] Xinwei Wang, Siwei Zhao, Hao Wang, and Tingrui Pan. Bubble formation on superhydrophobic-micropatterned copper surfaces. *Applied Thermal Engineering*, 35:112–119, 2012.

[12] Dong Song, Robert J Daniello, and Jonathan P Rothstein. Drag reduction using superhydrophobic sanded teflon surfaces. *Experiments in fluids*, 55(8):1783, 2014.

[13] Hongyu Dong, Mengjiao Cheng, Yajun Zhang, Hao Wei, and Feng Shi. Extraordinary drag-reducing effect of a superhydrophobic coating on a macroscopic model ship at high speed. *Journal of Materials Chemistry A*, 1(19):5886–5891, 2013.

[14] Vahid Mortazavi and MM Khonsari. On the degradation of superhydrophobic surfaces: A review. *Wear*, 372:145–157, 2017.

[15] Xi Zhang, Feng Shi, Jia Niu, Yugui Jiang, and Zhiqiang Wang. Superhydrophobic surfaces: from structural control to functional application. *Journal of Materials Chemistry*, 18(6):621–633, 2008.

[16] Joonsik Park, Hyuneui Lim, Wandoo Kim, and Jong Soo Ko. Design and fabrication of a superhydrophobic glass surface with micro-network of nanopillars. *Journal of colloid and interface science*, 360(1):272–279, 2011.

[17] A Milionis, J Languasco, E Loth, and IS Bayer. Analysis of wear abrasion resistance of superhydrophobic acrylonitrile butadiene styrene rubber (abs) nanocomposites. *Chemical Engineering Journal*, 281:730–738, 2015.

[18] Peichun Tsai, Maurice HW Hendrix, Remko RM Dijkstra, Lingling Shui, and Detlef Lohse. Microscopic structure influencing macroscopic splash at high weber number. *Soft Matter*, 7(24):11325–11333, 2011.

[19] HangJin Jo, Kyung Won Hwang, DongHyun Kim, Moriyama Kiyofumi, Hyun Sun Park, Moo Hwan Kim, and Ho Seon Ahn. Loss of superhydrophobicity of hydrophobic micro/nano structures during condensation. *Scientific reports*, 5:9901, 2015.

[20] S Moulinet and D Bartolo. Life and death of a fakir droplet: Impalement transitions on superhydrophobic surfaces. *The European Physical Journal E*, 24(3):251–260, 2007.

[21] Daiki Murakami, Hiroshi Jinnai, and Atsushi Takahara. Wetting transition from the cassie–baxter state to the wenzel state on textured polymer surfaces. *Langmuir*, 30(8):2061–2067, 2014.

[22] Tai-min Cai, Zhi-hai Jia, Hui-nan Yang, and Gang Wang. Investigation of cassie-wenzel wetting transitions on microstructured surfaces. *Colloid and Polymer Science*, 294(5):833–840, 2016.

[23] Gang Wang, Zhi-hai Jia, and Hui-nan Yang. Stability of a water droplet on micropillared hydrophobic surfaces. *Colloid and Polymer Science*, 294(5):851–858, 2016.

[24] D. Brutin. *Droplet Wetting and Evaporation: From Pure to Complex Fluids*. Elsevier Science, 2015.

[25] P. Saramito. *Complex fluids: Modeling and Algorithms*. Mathématiques et Applications. Springer International Publishing, 2016.

[26] Jean-Christophe Baret. Surfactants in droplet-based microfluidics. *Lab on a Chip*, 12(3):422–433, 2012.

[27] Michele Zagnoni, Charles N Baroud, and Jonathan M Cooper. Electrically initiated upstream coalescence cascade of droplets in a microfluidic flow. *Physical Review E*, 80(4):046303, 2009.

[28] Jason G Kralj, Martin A Schmidt, and Klavs F Jensen. Surfactant-enhanced liquid–liquid extraction in microfluidic channels with inline electric-field enhanced coalescence. *Lab on a Chip*, 5(5):531–535, 2005.

[29] JH Xu, PF Dong, H Zhao, CP Tostado, and GS Luo. The dynamic effects of surfactants on droplet formation in coaxial microfluidic devices. *Langmuir*, 28(25):9250–9258, 2012.

[30] JH Xu, GS Luo, SW Li, and GG Chen. Shear force induced monodisperse droplet formation in a microfluidic device by controlling wetting properties. *Lab on a Chip*, 6(1):131–136, 2006.

[31] JH Xu, SW Li, J Tan, YJ Wang, and GS Luo. Controllable preparation of monodisperse o/w and w/o emulsions in the same microfluidic device. *Langmuir*, 22(19):7943–7946, 2006.

[32] Ana Egatz-Gómez, John Schneider, P Aella, Dongqing Yang, P Domínguez-García, Solitaire Lindsay, ST Picraux, Miguel A Rubio, Sonia Melle, Manuel Marquez, et al. Silicon nanowire and polyethylene superhydrophobic surfaces for discrete magnetic microfluidics. *Applied Surface Science*, 254(1):330–334, 2007.

[33] Lingfei Hong and Tingrui Pan. Surface microfluidics fabricated by photopatternable superhydrophobic nanocomposite. *Microfluidics and Nanofluidics*, 10(5):991–997, 2011.

[34] PE Oomen, JPSH Mulder, E Verpoorte, and RD Oleschuk. Controlled, synchronized actuation of microdroplets by gravity in a superhydrophobic, 3d-printed device. *Analytica chimica acta*, 988:50–57, 2017.

[35] Michele Ferrari, Francesca Ravera, Silvia Rao, and Libero Liggieri. Surfactant adsorption at superhydrophobic surfaces. *Applied physics letters*, 89(5):053104, 2006.

[36] Michele Ferrari and Francesca Ravera. Surfactants and wetting at superhydrophobic surfaces: Water solutions and non aqueous liquids. *Advances in colloid and interface science*, 161(1):22–28, 2010.

[37] Stephen US Choi and Jeffrey A Eastman. Enhancing thermal conductivity of fluids with nanoparticles. Technical report, Argonne National Lab., IL (United States), 1995.

[38] Rudolf Hergt, Silvio Dutz, Robert Müller, and Matthias Zeisberger. Magnetic particle hyperthermia: nanoparticle magnetism and materials development for cancer therapy. *Journal of Physics: Condensed Matter*, 18(38):S2919, 2006.

[39] Clement Kleinstreuer, Jie Li, and Junemo Koo. Microfluidics of nano-drug delivery. *International Journal of Heat and Mass Transfer*, 51(23):5590–5597, 2008.

[40] Cong Mao, Yong Huang, Xin Zhou, Hangyu Gan, Jian Zhang, and Zhixiong Zhou. The tribological properties of nanofluid used in minimum quantity lubrication grinding. *The International Journal of Advanced Manufacturing Technology*, 71(5-8):1221–1228, 2014.

[41] Tünde Borbáth, Doina Bica, Iosif Potencz, Ladislau Vékás, István Borbáth, and Tibor Boros. Magnetic nanofluids and magnetic composite fluids in rotating seal systems. In *IOP conference series: earth and environmental science*, volume 12, page 012105. IOP Publishing, 2010.

[42] Robert D Deegan, Olgica Bakajin, Todd F Dupont, Greb Huber, Sidney R Nagel, and Thomas A Witten. Capillary flow as the cause of ring stains from dried liquid drops. *Nature*, 389(6653):827–829, 1997.

[43] Mercy Dicuangco, Susmita Dash, Justin A Weibel, and Suresh V Garimella. Effect of superhydrophobic surface morphology on evaporative deposition patterns. *Appl. Phys. Lett.*, 104(20):201604, 2014.

[44] Saptarshi Basu, Lalit Bansal, and Ankur Miglani. Towards universal buckling dynamics in nanocolloidal sessile droplets: the effect of hydrophilic to superhydrophobic substrates and evaporation modes. *Soft matter*, 12(22):4896–4902, 2016.

[45] John Ballato and Andrew James. A ceramic photonic crystal temperature sensor. *Journal of the American Ceramic Society*, 82(8):2273–2275, 1999.

[46] Hiroshi Fudouzi and Tsutomu Sawada. Tuning stop band of soft opal film by deformation for strain sensing applications. In *Proc SPIE*, volume 6369, pages 63690D–1, 2006.

[47] Min Qiu, Mikael Mulot, Marcin Swillo, Srinivasan Anand, Bozena Jaskorzynska, Anders Karlsson, Martin Kamp, and Alfred Forchel. Photonic crystal optical filter based on contra-directional waveguide coupling. *Applied Physics Letters*, 83(25):5121–5123, 2003.

[48] Jeffrey B Chou, Yi Xiang Yeng, Andrej Lenert, Veronika Rinnerbauer, Ivan Celanovic, Marin Soljačić, Evelyn N Wang, and Sang-Gook Kim. Design of wide-angle selective absorbers/emitters with dielectric filled metallic photonic crystals for energy applications. *Optics express*, 22(101):A144–A154, 2014.

[49] Hatice Altug, Dirk Englund, and Jelena Vučković. Ultrafast photonic crystal nanocavity laser. *Nature Physics*, 2(7):484–488, 2006.

[50] Ertugrul Cubukcu, Koray Aydin, Ekmel Ozbay, Stavroula Foteinopoulou, and Costas M Soukoulis. Subwavelength resolution in a two-dimensional photonic-crystal-based superlens. *Physical review letters*, 91(20):207401, 2003.

[51] J.D. Joannopoulos, S.G. Johnson, J.N. Winn, and R.D. Meade. *Photonic Crystals: Molding the Flow of Light, Second Edition*. Princeton University Press, 2011.

[52] Min Guo, Keyu Xie, Yu Wang, Limin Zhou, and Haitao Huang. Aperiodic tio2 nanotube photonic crystal: full-visible-spectrum solar light harvesting in photovoltaic devices. *Scientific reports*, 4, 2014.

[53] Qihuang Gong and Xiaoyong Hu. *Photonic crystals: principles and applications*. CRC Press, 2014.

[54] Xiaoyan Zhou, Zhaozhu Zhang, Xianghui Xu, Fang Guo, Xiaotao Zhu, Xuehu Men, and Bo Ge. Robust and durable superhydrophobic cotton fabrics for oil/water separation. *ACS applied materials & interfaces*, 5(15):7208–7214, 2013.

[55] Changping Ruan, Kelong Ai, Xingbo Li, and Lehui Lu. A superhydrophobic sponge with excellent absorbency and flame retardancy. *Angewandte Chemie International Edition*, 53(22):5556–5560, 2014.

[56] Nan Wang, Dangsheng Xiong, Yaling Deng, Yan Shi, and Kun Wang. Mechanically robust superhydrophobic steel surface with anti-icing, uv-durability, and corrosion resistance properties. *ACS applied materials & interfaces*, 7(11):6260–6272, 2015.

[57] Ziqi Sun, Ting Liao, Kesong Liu, Lei Jiang, Jung Ho Kim, and Shi Xue Dou. Fly-eye inspired superhydrophobic anti-fogging inorganic nanostructures. *Small*, 10(15):3001–3006, 2014.

[58] Bichitra Nanda Sahoo and Balasubramanian Kandasubramanian. Recent progress in fabrication and characterisation of hierarchical biomimetic superhydrophobic structures. *Rsc Advances*, 4(42):22053–22093, 2014.

[59] Shen Yu, Zhiguang Guo, and Weimin Liu. Biomimetic transparent and superhydrophobic coatings: from nature and beyond nature. *Chemical Communications*, 51(10):1775–1794, 2015.

[60] Jau-Ye Shiu, Chiung-Wen Kuo, Wha-Tzong Whang, and Peilin Chen. Observation of enhanced cell adhesion and transfection efficiency on superhydrophobic surfaces. *Lab on a Chip*, 10(5):556–558, 2010.

[61] Jau-Ye Shiu, Chiung Wen Kuo, Wha-Tzong Whang, and Peilin Chen. Addressable cell microarrays via switchable superhydrophobic surfaces. *Journal of Adhesion Science and Technology*, 24(5):1023–1030, 2010.

[62] Zong-Han Yang, Fan-Ching Chien, Chiung-Wen Kuo, Di-Yen Chueh, and Peilin Chen. Hybrid contact and interfacial adhesion on well-defined periodic hierarchical pillars. *Nanoscale*, 5(3):1018–1025, 2013.

[63] Aurélien F Stalder, Tobias Melchior, Michael Müller, Daniel Sage, Thierry Blu, and Michael Unser. Low-bond axisymmetric drop shape analysis for surface tension and contact angle measurements of sessile drops. *Colloids and Surfaces A: Physicochemical and Engineering Aspects*, 364(1):72–81, 2010.

[64] J Bico, C Tordeux, and D Quéré. Rough wetting. *EPL (Europhysics Letters)*, 55(2):214–220, 2001.

[65] Adrien Bussonniére, Masoud B Bigdeli, Di-Yen Chueh, Qingxia Liu, Peilin Chen, and Peichun Amy Tsai. Universal wetting transition of an evaporating water droplet on hydrophobic micro-and nano-structures. *Soft matter*, 13(5):978–984, 2017.

[66] YC Jung and B Bhushan. Wetting behaviour during evaporation and condensation of water microdroplets on superhydrophobic patterned surfaces. *Journal of microscopy*, 229(1):127–140, 2008.

[67] Laura Barbieri, Estelle Wagner, and Patrik Hoffmann. Water wetting transition parameters of perfluorinated substrates with periodically distributed flat-top microscale obstacles. *Langmuir*, 23(4):1723–1734, 2007.

[68] Aurélie Lafuma and David Quéré. Superhydrophobic states. *Nat. Mater.*, 2(7):457, 2003.

[69] Alberto Giacomello, Mauro Chinappi, Simone Meloni, and Carlo Massimo Casciola. Metastable wetting on superhydrophobic surfaces: continuum and atomistic views of the cassie-baxter–wenzel transition. *Physical review letters*, 109(22):226102, 2012.

[70] Anish Tuteja, Wonjae Choi, Minglin Ma, Joseph M Mabry, Sarah A Mazzella, Gregory C Rutledge, Gareth H McKinley, and Robert E Cohen. Designing superoleophobic surfaces. *Science*, 318(5856):1618–1622, 2007.

[71] Satoshi Shibuichi, Tomohiro Onda, Naoki Satoh, and Kaoru Tsujii. Super water-repellent surfaces resulting from fractal structure. *The Journal of Physical Chemistry*, 100(50):19512–19517, 1996.

[72] David Quéré. Wetting and roughness. *Annu. Rev. Mater. Res.*, 38:71–99, 2008.

[73] Xuemei Chen, Ruiyuan Ma, Jintao Li, Chonglei Hao, Wei Guo, Bing Lam Luk, Shuai Cheng Li, Shuhuai Yao, and Zuankai Wang. Evaporation of droplets on superhydrophobic surfaces: Surface roughness and small droplet size effects. *Physical review letters*, 109(11):116101, 2012.

[74] AJB Milne and A Amirfazli. The cassie equation: How it is meant to be used. *Advances in colloid and interface science*, 170(1):48–55, 2012.

[75] Edward Bormashenko. Wetting transitions on biomimetic surfaces. *Philosophical Transactions of the Royal Society of London A: Mathematical, Physical and Engineering Sciences*, 368(1929):4695–4711, 2010.

[76] Glen McHale, Sanaa Aqil, NJ Shirtcliffe, MI Newton, and H Yildirim Erbil. Analysis of droplet evaporation on a superhydrophobic surface. *Langmuir*, 21(24):11053–11060, 2005.

[77] S Dash, N Kumari, and SV Garimella. Characterization of ultrahydrophobic hierarchical surfaces fabricated using a single-step fabrication methodology. *Journal of Micromechanics and Microengineering*, 21(10):105012, 2011.

[78] Feng-Chao Wang and Heng-An Wu. Pinning and depinning mechanism of the contact line during evaporation of nano-droplets sessile on textured surfaces. *Soft Matter*, 9(24):5703–5709, 2013.

[79] Chi Young Lee, Bong June Zhang, Jiyeon Park, and Kwang J Kim. Water droplet evaporation on cu-based hydrophobic surfaces with nano-and micro-structures. *International Journal of Heat and Mass Transfer*, 55(7):2151–2159, 2012.

[80] Wei Xu, Rajesh Leeladhar, Yong Tae Kang, and Chang-Hwan Choi. Evaporation kinetics of sessile water droplets on micropillared superhydrophobic surfaces. *Langmuir*, 29(20):6032–6041, 2013.

[81] François J. Peaudecerf, Julien R. Landel, Raymond E. Goldstein, and Paolo Luzzatto-Fegiz. Traces of surfactants can severely limit the drag reduction of superhydrophobic surfaces. *Proceedings of the National Academy of Sciences*, 114(28):7254–7259, 2017.

[82] R Mohammadi, J Wassink, and A Amirfazli. Effect of surfactants on wetting of super-hydrophobic surfaces. *Langmuir*, 20(22):9657–9662, 2004.

[83] Zhiliang Zhang and Weiyue Zhu. Controllable fabrication of a flexible transparent metallic grid conductor based on the coffee ring effect. *J. Mater. Chem. C*, 2(45):9587–9591, 2014.

[84] Kanna Aoki, Denis Guimard, Masao Nishioka, Masahiro Nomura, Satoshi Iwamoto, and Yasuhiko Arakawa. Coupling of quantum-dot light emission with a three-dimensional photonic-crystal nanocavity. *Nat. Photonics*, 2(11):688–692, 2008.

[85] Masoud Bozorg Bigdeli and Matteo Fasano. Thermal transmittance in graphene based networks for polymer matrix composites. *Int. J. Therm. Sci.*, 117:98–105, 2017.

[86] Masoud Bozorg Bigdeli, Matteo Fasano, Annalisa Cardellini, Eliodoro Chiavazzo, and Pietro Asinari. A review on the heat and mass transfer phenomena in nanofluid coolants with special focus on automotive applications. *Renew. Sustain. Energy Rev.*, 60:1615–1633, 2016.

[87] A Syed, L Mangano, P Mao, J Han, and Y-A Song. Creating sub-50 nm nanofluidic junctions in a pdms microchip via self-assembly process of colloidal silica beads for electrokinetic concentration of biomolecules. *Lab Chip*, 14(23):4455–4460, 2014.

[88] Geoffrey A Ozin, Kun Hou, Bettina V Lotsch, Ludovico Cademartiri, Daniel P Puzzo, Francesco Scotognella, Arya Ghadimi, and Jordan Thomson. Nanofabrication by self-assembly. *Mater. Today*, 12(5):12–23, 2009.

[89] Wonmok Lee, Angel Chan, Michael A Bevan, Jennifer A Lewis, and Paul V Braun. Nanoparticle-mediated epitaxial assembly of colloidal crystals on patterned substrates. *Langmuir*, 20(13):5262–5270, 2004.

[90] Ahmet Faik Demirörs, Patrick M. Johnson, Carlos M. van Kats, Alfons van Blaaderen, and Arnout Imhof. Directed self-assembly of colloidal dumbbells with an electric field. *Langmuir*, 26(18):14466–14471, 2010.

[91] Tao Ding, Kai Song, Koen Clays, and Chen-Ho Tung. Fabrication of 3d photonic crystals of ellipsoids: Convective self-assembly in magnetic field. *Adv. Mater.*, 21(19):1936–1940, 2009.

[92] Yuanjin Zhao, Luoran Shang, Yao Cheng, and Zhongze Gu. Spherical colloidal photonic crystals. *Acc. Chem. Res.*, 47(12):3632–3642, 2014.

[93] Hanbin Zheng and Serge Ravaine. Bottom-up assembly and applications of photonic materials. *Crystals*, 6(5):54, 2016.

[94] Ankur Miglani and Saptarshi Basu. Sphere to ring morphological transformation in drying nanofluid droplets in a contact-free environment. *Soft Matter*, 11(11):2268–2278, 2015.

[95] Jingxia Wang, Libin Wang, Yanlin Song, and Lei Jiang. Patterned photonic crystals fabricated by inkjet printing. *J. Mater. Chem. C*, 1(38):6048–6058, 2013.

[96] Ming-Yu Zhang, Ke Xu, Jian-Hong Xu, and Guang-Sheng Luo. Self-assembly kinetics of colloidal particles inside monodispersed micro-droplet and fabrication of anisotropic photonic crystal micro-particles. *Crystals*, 6(10):122, 2016.

[97] Elena Celia, Thierry Darmanin, Elisabeth Taffin de Givenchy, Sonia Amigoni, and Frédéric Guittard. Recent advances in designing superhydrophobic surfaces. *J. Colloid Interface Sci.*, 402:1–18, 2013.

[98] H Yildirim Erbil. Evaporation of pure liquid sessile and spherical suspended drops: A review. *Adv. Colloid Interface Sci.*, 170(1):67–86, 2012.

[99] M Reyssat, JM Yeomans, and D Quéré. Impalement of fakir drops. *EPL*, 81(2):26006, 2007.

[100] Angelo Accardo, Francesco Gentile, Federico Mecarini, Francesco De Angelis, Manfred Burghammer, Enzo Di Fabrizio, and Christian Riekel. In situ x-ray scattering studies of protein solution droplets drying on micro-and nanopatterned superhydrophobic pmma surfaces. *Langmuir*, 26(18):15057–15064, 2010.

[101] Álvaro G Marín, Hanneke Gelderblom, Arturo Susarrey-Arce, Arie van Houselt, Leon Lefferts, Johannes GE Gardeniers, Detlef Lohse, and Jacco H Snoeijer. Building microscopic soccer balls with evaporating colloidal fakir drops. *Proc. Natl. Acad. Sci. U.S.A.*, 109(41):16455–16458, 2012.

[102] Philippe Brunet. Particle deposition after droplet evaporation on ultra-hydrophobic micro-textured surfaces. *Soft Matter*, 8(44):11294–11301, 2012.

[103] Angelo Accardo, Francesco Di Stasio, Manfred Burghammer, Christian Riekel, and Roman Krahne. Nanocrystal self-assembly into hollow dome-shaped microstructures by slow solvent evaporation on superhydrophobic substrates. *Part. Part. Syst. Charact.*, 32(5):524–528, 2015.

[104] L Pauchard and Y Couder. Invagination during the collapse of an inhomogeneous spheroidal shell. *EPL*, 66(5):667, 2004.

[105] Lifeng Chen and Julian RG Evans. Drying of colloidal droplets on superhydrophobic surfaces. *J. Colloid Interface Sci.*, 351(1):283–287, 2010.

[106] Peichun Tsai, Rob GH Lammertink, Matthias Wessling, and Detlef Lohse. Evaporation-triggered wetting transition for water droplets upon hydrophobic microstructures. *Phys. Rev. Lett.*, 104(11):116102, 2010.

[107] Céline Sadek, Hervé Tabuteau, Pierre Schuck, Yannick Fallourd, Nicolas Pradeau, Cécile Le Floch-Fouéré, and Romain Jeantet. Shape, shell, and vacuole formation during the drying of a single concentrated whey protein droplet. *Langmuir*, 29(50):15606–15613, 2013.

[108] H Mıguez, C Lopez, F Meseguer, A Blanco, L Vazquez, R Mayoral, M Ocana, V Fornes, and A Mifsud. Photonic crystal properties of packed submicrometric SiO_2 spheres. *Appl. Phys. Lett.*, 71(9):1148–1150, 1997.

[109] LV Woodcock. Entropy difference between the face-centred cubic and hexagonal close-packed crystal structures. *Nature*, 385(6612):141, 1997.

[110] Noriyuki Suzuki, Eiji Iwase, and Hiroaki Onoe. Microfluidically patterned dome-shaped photonic colloidal crystals exhibiting structural colors with low angle dependency. *Adv. Opt. Mater.*, 5(4), 2017.

[111] Fangfang Liu, Jinghai Xiu, Bingtao Tang, Defeng Zhao, and Shufen Zhang. Dynamic monitoring of thermally assisted assembly of colloidal crystals. *J. Mater. Sci.*, 52(13):7883–7892, 2017.

[112] Jae-Hyuck Yoo, Hyuk-Jun Kwon, Dongwoo Paeng, Junyeob Yeo, Selim Elhadj, and Costas P Grigoropoulos. Facile fabrication of a superhydrophobic cage by laser direct writing for site-specific colloidal self-assembled photonic crystal. *Nanotechnology*, 27(14):145604, 2016.

[113] Geoffrey A Ozin, André C Arsenault, and Ludovico Cademartiri. *Nanochemistry: a chemical approach to nanomaterials*. Royal Society of Chemistry, 2009.